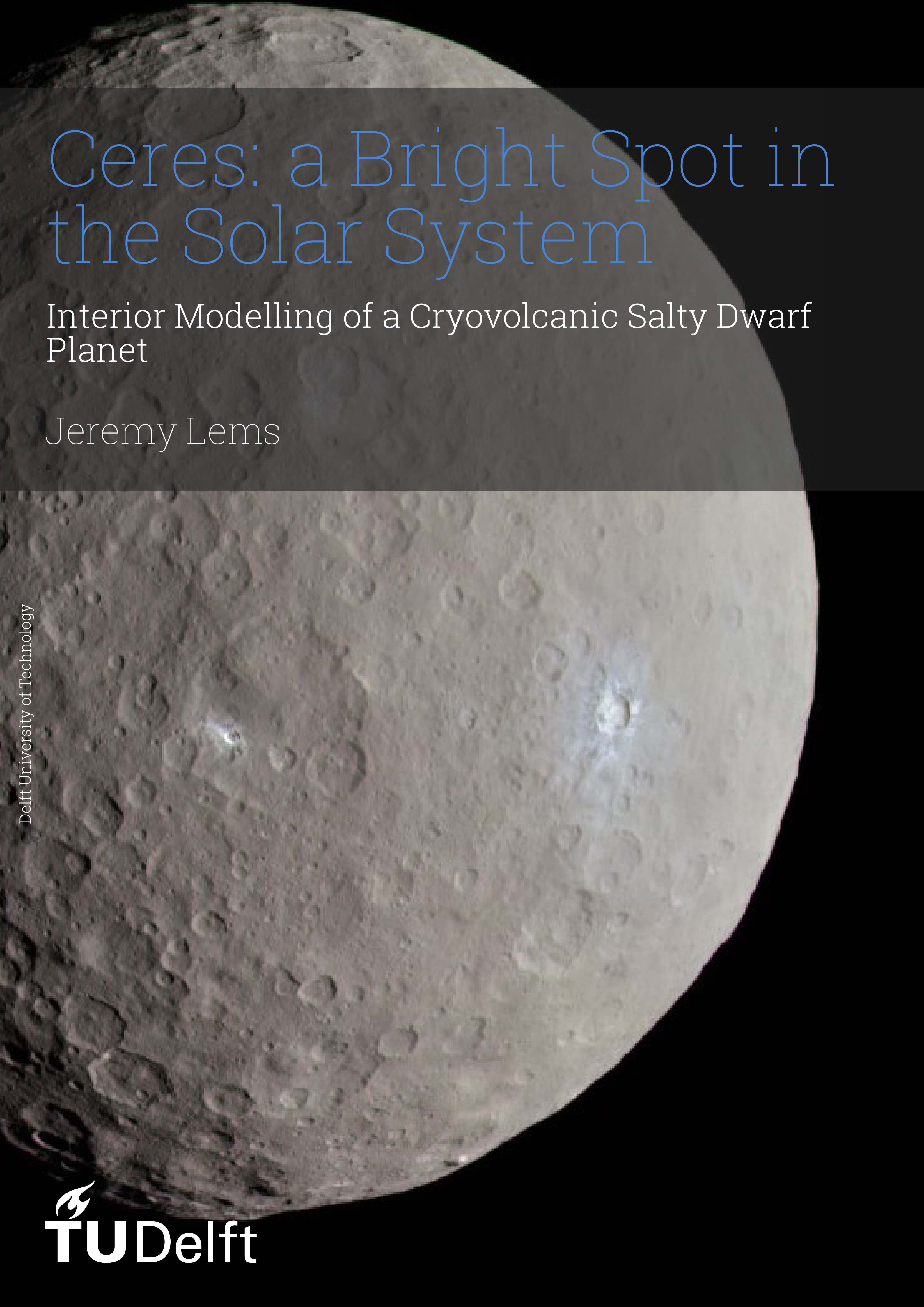

Ceres: a Bright Spot in the Solar System

Interior Modelling of a Cryovolcanic Salty Dwarf Planet

Jeremy Lems

Delft University of Technology

TUDelft

Ceres: a Bright Spot in the Solar System

Interior Modelling of a Cryovolcanic Salty Dwarf Planet

by

Jeremy Lems

Supervisor:	Dr. Ir. Bart C. Root
Faculty:	Faculty of Aerospace Engineering, Delft
Cover credits:	NASA's DAWN

TU Delft

Preface

This report is the capstone thesis for my MSc in Aerospace Engineering. It is an investigation of the interior of Ceres and the mechanism behind the cryovolcanic activity hypothesized to be happening there. Readers particularly interested in the interior models can find these in chapter 3, and the benchmarking of isostasy-based crust models is done in chapter 4.

It feels rather strange to be finishing off this final phase of my university education. What for the longest time seemed like an insurmountable task is now all but surmounted, and I must admit that there were many times I felt like I would never arrive at this point. I am reminded of participating in the selection procedure for this program, more than six years ago now, and how much has happened since then. Though I didn't know it at the time, I was about to start on the most difficult thing I had ever done. Looking back, however, I am glad it was so challenging, as it allowed me to overcome my own self-doubt, and to achieve more self-growth than I ever thought possible. I had never in my wildest dreams imagined that it would be this difficult and that I would still be able to do it, and yet here I am.

I must express my deepest gratitude and appreciation to my supervisor, Bart Root, who has provided me with unparalleled guidance and support throughout this project. Working with him made this thesis project a uniquely enjoyable and positive experience, and has allowed me to produce a work that I am truly proud of on a topic I am deeply passionate about. I would like to thank my friends and family for their contributions to my enjoyment of the project and for allowing me to rant about why I think Ceres is so cool. In particular, I would like to thank my mother, who has always believed in me even when I myself couldn't.

Jeremy Lems
Delft, September 2024

Abstract

Ceres is a small dwarf planet in the asteroid belt between Mars and Jupiter, at 2.77 AU from the Sun. Its position in the solar system makes it a unique body, as it makes it unclear if its interior is analogous to a terrestrial or an icy body. Only one mission, the DAWN mission, has gone to Ceres to collect data. One of the most puzzling of its features are the bright spots on its surface, which have long been conjectured to be the result of cryovolcanic activity involving salt water. In this work, Ceres' interior was studied to investigate the mechanism by which these bright spots form. Greater understanding of this mechanism will increase the scientific knowledge on how unique planetary interiors and cryovolcanism can function.

Ceres' internal density structure was found by constraining its interior using measurements of its mass and mean mass moment of inertia. This was supplemented by using gravity measurements to develop crust models, the parameters of which were linked to the parameters of the density structure, to provide a final constraint to the density profile. For reasons of parsimony, a 2-layer density structure was assumed.

Two different isostasy-based crust models were developed, using either Pratt or Airy compensation. The Pratt model has a crust thickness of 70 km and densities varying between 1300 kg/m^3 and 1800 kg/m^3, whereas the Airy model has a crust density of 1310 kg/m^3 and thicknesses varying between 24 km and 57 km. The corresponding mantle densities are 2520 kg/m^3 and 2410 kg/m^3 for the Pratt and Airy model, respectively. The performance of isostasy-based crust models were investigated using measurements of Moho depth on Earth, and they are expected to be able to predict crustal properties with a mean error of 13.5%. The temperature in Ceres' interior was modelled assuming no flow and only radiogenic heating as a heat source.

No significant correlation was found between the observed locations of cryovolcanism and crustal properties for any of the models, implying that the brine involved in the formation of the bright spots is homogeneously distributed throughout the crust. Furthermore, it was found that the temperature at the base of the crust is likely high enough to allow for liquid brines to be present without the need for impact heating.

Therefore, it is hypothesized that Ceres has a muddy ocean layer between the crust and the mantle, which is the source of the brines which form bright spots on its surface. Impacts would then form cracks in the crust, which would allow for this brine to rise to the surface. Recommended for future work is to investigate the process by which these brines are driven to the surface, and to include the effects of the muddy ocean on the temperature profile in Ceres' interior.

Contents

Nomenclature

Abbreviations

Abbreviation	Definition
RMSE	Root-mean-square error

Symbols

Symbol	Definition	Unit
A_b	Bond albedo	-
C_p	Heat capacity	J/K
c_f	Freezing point depression constant	K/mol
D	Flexural rigidity of the elastic lithosphere	Nm^2
E	Young's modulus of lithosphere material	Pa
F_{sun}	Solar constant	W/m^2
f_s	Serpentinite mass fraction	-
G	Gravitational constant	Nm^2/kg^2
H	Volumetric radiogenic heating rate	W/m^3
g	Gravitational acceleration	m/s^2
h_b	Deviation from reference depth (positive downwards)	m
h_t	Topography at the top of the crust	m
I	Planetary mass moment of inertia	$kg{\cdot}m^2$
I_{norm}	Normalized moment of inertia	-
J_2	Strength of the gravitational effect of the equatorial bulge	-
i	Number of particles formed when solute dissolves	-
K	Bulk modulus	Pa
k	Thermal conductivity	W/mK
M	Planetary mass	kg
M_{molar}	Molar mass	kg/mol
m	Local mass	kg
m_{solute}	Dissolved solute mass	kg
n	Spherical harmonic degree	-
p	Local pressure	Pa
Δp	Pressure difference	Pa
q_r	ratio of the centrifugal acceleration to the gravitational acceleration	-
R	Planetary radius	m
r	Local radius	m
$r_{sun_{AU}}$	Distance from the sun	AU
S	Shear modulus of lithosphere material	Pa
T	Local temperature	K
T_e	Elastic lithosphere thickness	m
T_{ref}	Reference thickness for Pratt model	m
ΔT	Temperature difference	K
V	Planetary volume	m^3

Symbol	Definition	Unit
α_T	Thermal expansion coefficient	K^{-1}
$\Delta\rho$	Density contrast between crust and mantle	kg/m^3
ΔT_f	Freezing point depression	K
ϵ	Thermal emissivity	-
κ	Thermal diffusivity	m^2/s
μ	molality of solution	mol
ν	Poisson ratio of lithospheric material	-
ρ	Local density	kg/m^3
ρ_0	Nominal density	kg/m^3
ρ_c	Density of crust material	kg/m^3
ρ_m	Density of the mantle material	kg/m^3
ρ_{ref}	Reference density for Pratt model	kg/m^3
σ	Stefan-Boltzmann constant	W/m^{2}K^4
ω_{rot}	Angular velocity	rad/s

Subscripts

Subscript	Definition
0	Nominal value
b	Relating to the bottom of the crust
bound	Relating to the crust-mantle boundary
c	Relating to the crust
e	Relating to the elastic lithosphere
f	Relating to the freezing point
i	Relating to ice
m	Relating to the mantle
norm	Normalized value
rot	Relating to rotation
s	Relating to serpentinite
solute	Relating to the solute of a solution
solvent	Relating to the solvent of a solution
surface	Relating to the surface of Ceres
t	Relating to the top of the crust

1 Introduction

Ceres is a small dwarf planet in the asteroid belt between the orbits of Mars and Jupiter, at 2.77 AU (Lissauer & de Pater, 2019). It is the largest object in the asteroid belt, and the only one rounded by its own gravity. Its position in the solar system makes it colder than the terrestrial planets of the inner solar system, and yet warmer than the icy moons observed in the outer solar system. Its lack of thermally analogous bodies complicates the matter of studying its internal structure and geological processes, but also makes them all the more interesting. It has a particularly low bulk density compared to other terrestrial bodies, as shown in Figure 1.1. This implies that its composition is different from other terrestrial planets. Furthermore, its mean moment of inertia is approximately 0.37 (Park et al., 2016), implying it's not homogeneous but also not completely differentiated. Finally, one of the most puzzling of Ceres' features are the bright spots visible on it's surface, like the one in Occator crater, shown in Figure 1.2.

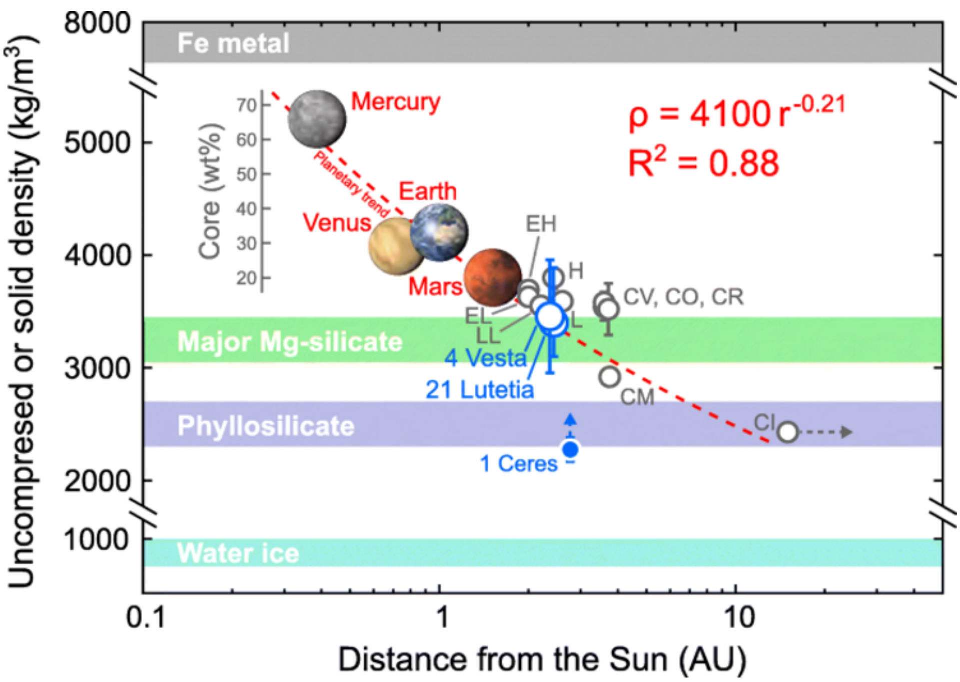

Figure 1.1: Bulk density of Ceres compared to other terrestrial bodies (McDonough & Yoshizaki, 2021).

In the rest of this chapter the current most up-to-date knowledge on Ceres is summarized, a research gap is identified, research questions are synthesized, and their relevance is discussed

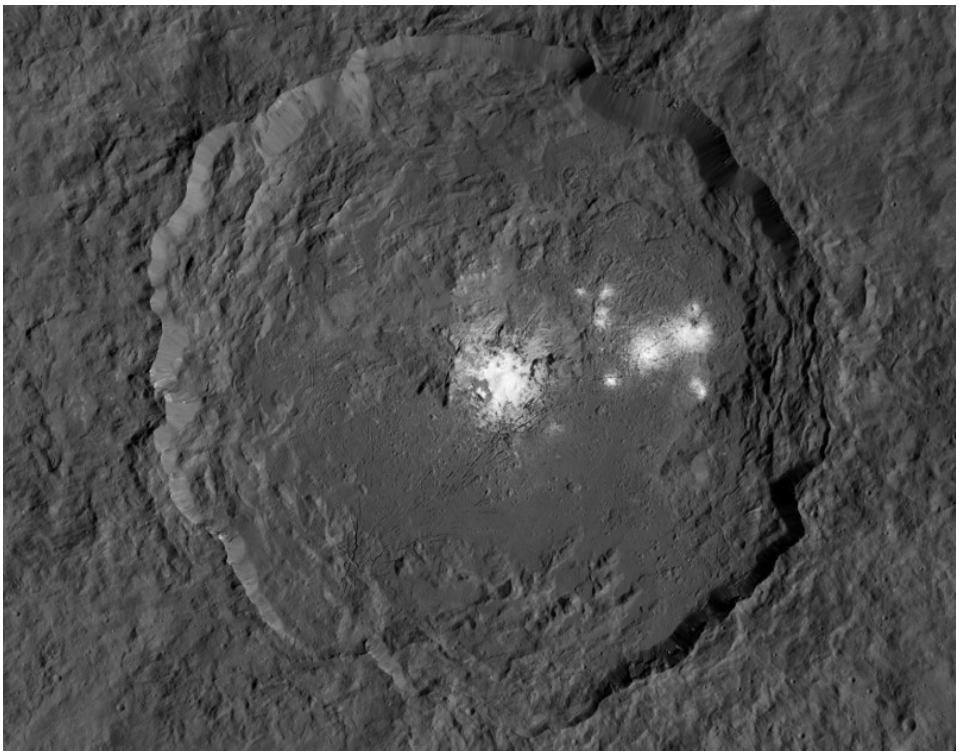

Figure 1.2: Bright spots in Occator crater. Image credits: NASA JPL.

One of the core questions about Ceres' interior is to what degree it is differentiated. Before the DAWN mission (2015), Thomas et al. (2005) determined that Ceres' shape is not consistent with that expected of a homogeneous body and must be (at least partially) differentiated. Meanwhile, McCord and Sotin (2005) modelled the internal radiogenic heating of the dwarf planet and came up with four different possible internal structures depending on different evolution scenarios. These models range from completely homogeneous to completely differentiated with an iron core, because this is dependent on the amount of internal heating and the internal composition. Zolotov (2009), on the other hand, argues that the measurements on Ceres' shape do not exclude the possibility of a homogeneous, gradually compacted interior. With the help of newly acquired topography and gravity data from DAWN, Neumann et al. (2015) found in an accretion study that it is very unlikely for Ceres to have maintained significant porosity until present. Castillo-Rogez and McCord (2010) then continued their research on Ceres' differentiation through radiogenic heating. The evolution scenarios they found are summarized in Figure 1.3. Here it can be seen that Ceres ends up with a three-layer structure under quite a number of evolution scenarios and that a metallic core forms in only one. Neumann et al. (2020) made a similar chart of evolution scenarios after doing another accretion study, constrained by newly acquired gravity and shape data from the DAWN mission and including a water mantle, shown in Figure 1.4. This figure shows that there are quite a number of possibilities for Ceres' interior structure, depending on which processes shape it. Many of these possible structures include a water layer. Castillo-Rogez and McCord distinguish different starting conditions, whereas Neumann distinguishes different internal processes that lead to various outcomes. In general, there is no consensus on how differentiated Ceres is, but most research agrees that it is unlikely that Ceres is completely differentiated and more likely that it is a partial differentiation, where layers differ in the relative content of ice, silicates and salts. Ceres' age is similarly not agreed upon, but usually an age of 5 million years is taken.

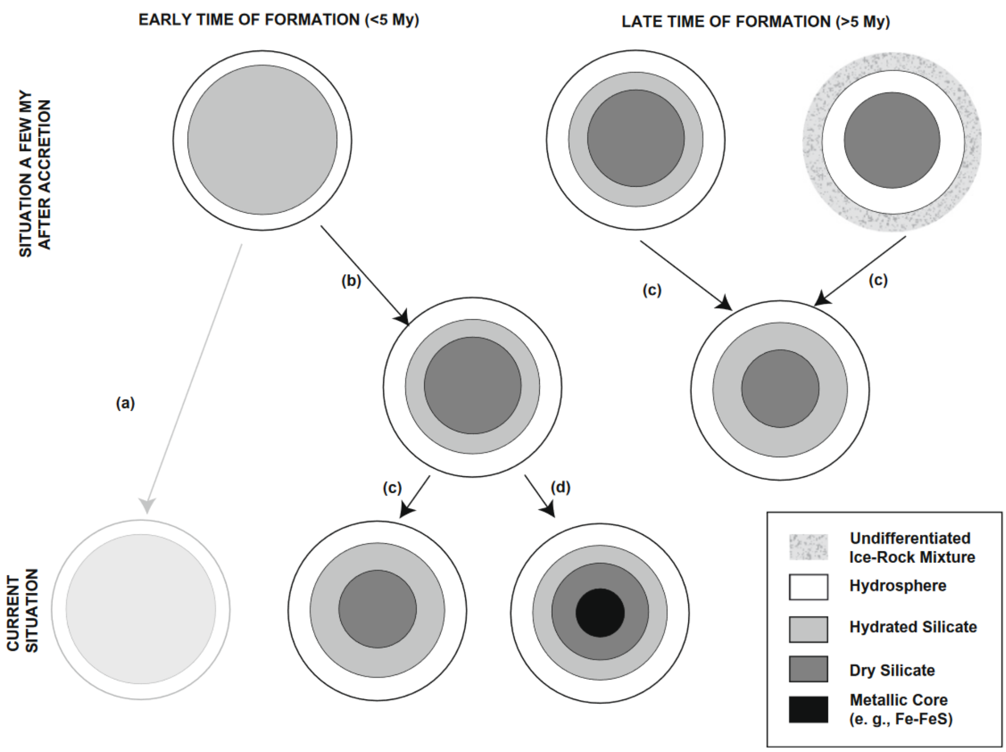

Figure 1.3: Possible interior structures of Ceres for different evolution scenarios (Castillo-Rogez & McCord, 2010).

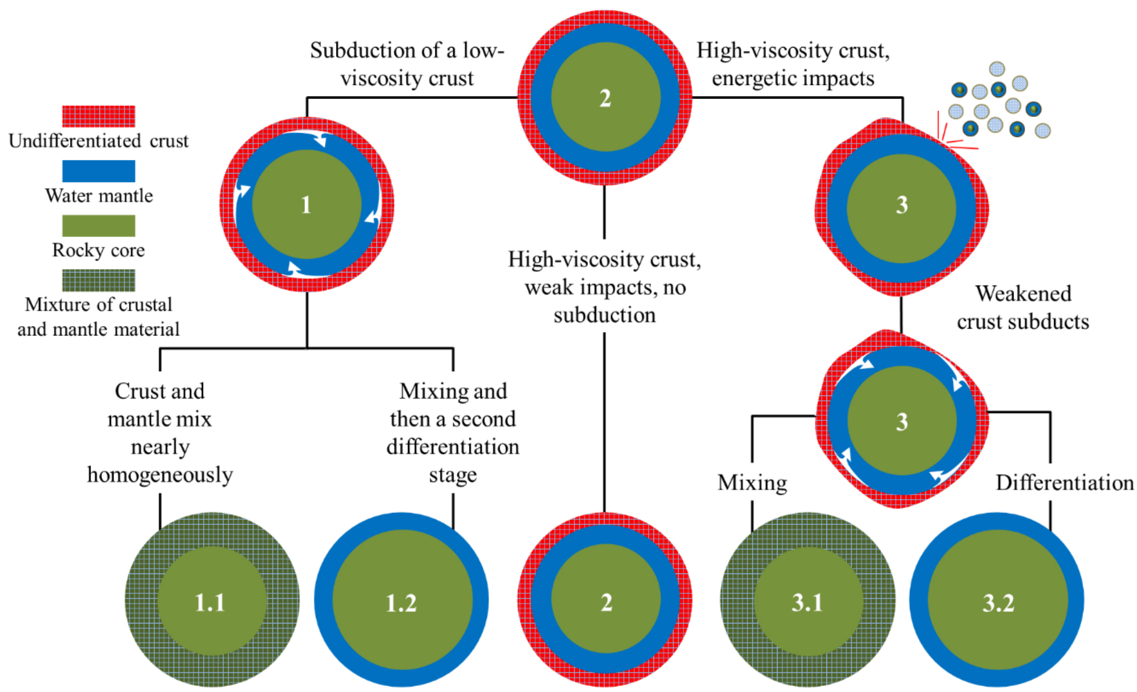

Figure 1.4: Possible interior structures of Ceres for different evolution scenarios (Neumann et al., 2020).

Many studies on the internal densities of Ceres assume a 2-layer structure to ensure parsimony, but the actual internal structure is not sufficiently constrained to draw conclusions about the deep interior. The results of many of these studies are summarized in Table 1.1, together with the average of the results obtained after the DAWN mission. Here it can be seen that in general the results are quite similar, especially post-DAWN. Furthermore, it is observed that the crust is expected to be almost two times lighter than the mantle with a relatively thin crust compared to the mantle. It should be carefully noted that the conventional meanings ascribed to words such as crust, mantle, and core in the inner solar system's terrestrial planets do not apply to Ceres, as its internal temperature and pressure are so low that it's interior is not expected to behave in the same way as those of the inner rocky planets. In this work, the terms mantle and crust will be used for the inner and outer layers, respectively. This decision is quite arbitrary, but it allows the reservation of the term core for a potential deeper layer in Ceres.

Table 1.1: Thicknesses and densities of 2-layer models in literature.

Source	ρ_{mantle} kg/m^3	ρ_{crust} kg/m^3	t_{crust} km
Thomas et al. (2005)	2700-3700	918	66-124
Tricarico (2014)	2400-3100	900-950	30-90
Neveu and Desch (2015)	2900	1430	107
Park et al. (2016)	2460-2900	1680-1950	70-190
Ermakov et al. (2017)	2426-2439	1200-1357	36.3-44.2
King et al. (2018)	2341-2393	1380-1440	35-40
Konopliv et al. (2018)	2260-2470	1200-1600	27-43
Average post-DAWN	2461	1476	60.7

An important parameter for the interior processes of the Dwarf planet is how hot it is on the inside. Many researchers have come up with temperature profiles from thermal evolution studies, and some have deduced temperatures necessary at specific depths to allow for brine deposits to be fluid and cause cryovolcanism. The first thermal profile was made by McCord and Sotin (2005) through their radiogenic heating model. The thermal profiles in Figure 1.5, which include a convecting mantle, indicate different times by line style. Usually, researchers instead display it in a 3-dimensional plot with the radius and the time as the axes, as shown in the thermal evolution model by Castillo-Rogez et al. (2019) in Figure 1.6 made by including a convective mud layer in their internal structure. Figure 1.5 shows that the core temperature starts at around 650 K and that it first increases to about 800 K and then decreases over time to approximately 325 K. The vertical part of the graph close to the surface indicates a convective layer. Because many researchers include several of these graphs for different initial conditions or assumptions, and they generally look quite similar, they will not be explicitly included here. Many thermal evolution models show the hottest temperatures late in Ceres' evolution; this is caused by the fact that Ceres is so small that the heat generated by accretion is less influential than that generated by radiogenic heating (Castillo-Rogez & McCord, 2010; Castillo-Rogez et al., 2019).

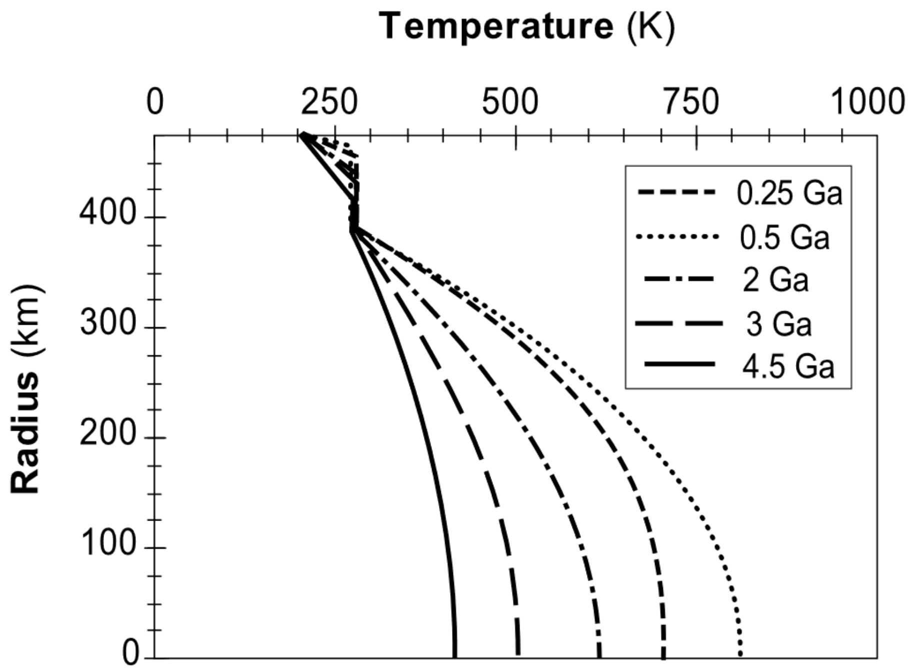

Figure 1.5: Thermal profiles for differentiated interior from the thermal evolution study of McCord and Sotin (2005).

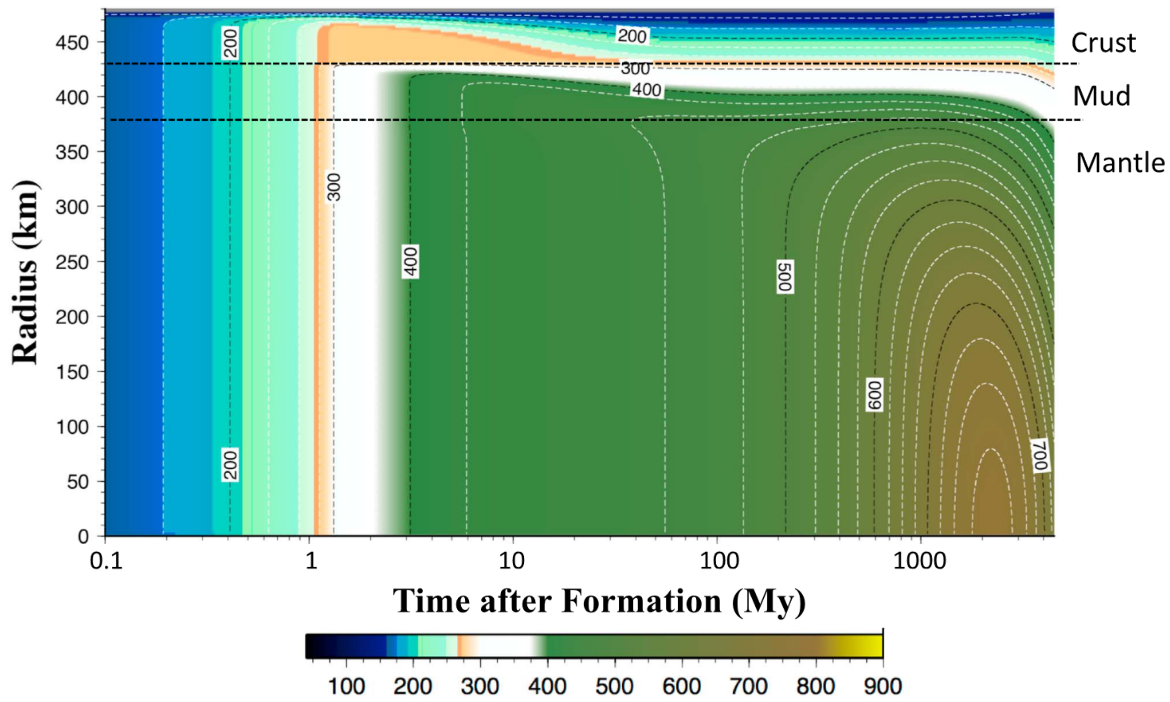

Figure 1.6: A 3-dimensional thermal evolution plot of Ceres interior model with mud layer (Castillo-Rogez et al., 2019).

Data from DAWN also allows for a determination of the surface composition. In particular, the observation of the bright spots opened up opportunities for the exploration of what these bright spots were made of. This was done by De Sanctis et al. (2016), who did an analysis of the spectral absorptance of the bright spots in Occator crater to find that they are most likely made largely of sodium carbonates with smaller amounts of ammonium carbonate or ammonium chloride. McCord and Zambon (2019) did a similar study of the entire surface and found that the surface shows a fairly uniform and widespread distribution of NH4- and Mg-phyllosilicates and carbonates. This was verified by De Angelis et al. (2021), who found that Mg-phyllosilicates are the best candidates for the ammonium-bearing species on Ceres' surface. These surface components could be related to the briny substance involved in the formation of the bright spots.

The composition of the deeper interior of Ceres is more difficult to study, as there is no way to observe it directly. However, studies on the required viscosity to match observations of relaxation on Ceres' surface can hold clues as to what composition is expected. Bland et al. (2016) found through numerical modelling of crater relaxation that Ceres' shallow subsurface is made up of no more than 30% to 40% ice by volume, with a mixture of rock, salt, and/or clathrates making up the rest. In a similar study, Fu et al. (2017) discovered that Ceres' crust is <25 vol.% water ice, <36 vol.% phyllosilicates or carbonates, and >29 vol.% low-density, high-strength phases such as salts. In order for mantle material to be able to rise to the surface in cryovolcanic activity, Ruesch et al. (2019) argue that the mantle must be made of a convective slurry with about 30-45 vol.% of non-soluble, solid particles.

It is widely accepted that there is cryovolcanic activity on Ceres that involves brines as an explanation for the observation of bright spots on Ceres' surface. Neveu and Desch (2015) hypothesized that Ceres' bright spots are manifestations of effusion of solute-bearing liquid extruded to the surface by the pressurization of ongoing freezing of a reservoir at the crust-mantle boundary where the temperature is similar to the eutectic temperature of the liquid. This hypothesis was later investigated and verified by Quick et al. (2019) by calculations on reservoir cooling. Ahuna Mons, a 4 kilometer high mountain on Ceres, was identified by Ruesch et al. (2016) to be a cryovolcano resulting from the upwelling of hydrated salts with a low eutectic temperature in the geologically recent past. Sori et al. (2017) argued that cryovolcanic structures induce relaxation on Ceres' surface that renders them unidentifiable within geologically short timespans, explaining why not many of these structures are found on Ceres' surface today. By experimenting with the freezing of several compositions of brines, Vu et al. (2017) found that to produce that material found in the bright spots, the material from which they form must be either rich in ammonium or chloride, or both. Following from their thermal evolution models, Castillo-Rogez et al. (2019) inferred that the preservation of a brine reservoir at the crust-mantle boundary is possible if the crust is rich in clathrate hydrates, for which the temperature at the boundary exceeds 220 Kelvin. Stein et al. (2019) researched the formation mechanisms of bright spots and discovered that they are formed through impact-induced heating and upwelling of volatile-rich materials or the excavation of heterogeneously distributed subsurface brines.

These formation mechanisms are illustrated in Figure 1.7. In mechanism A, impact heating melts brines that are present close to the surface, whereas in mechanism B the impacts form cracks that reach subsurface brine pockets. Due to the seemingly random presence of bright spots in craters, formation mechanism B is considered more likely, as this explains why some craters would have bright spots and others wouldn't.

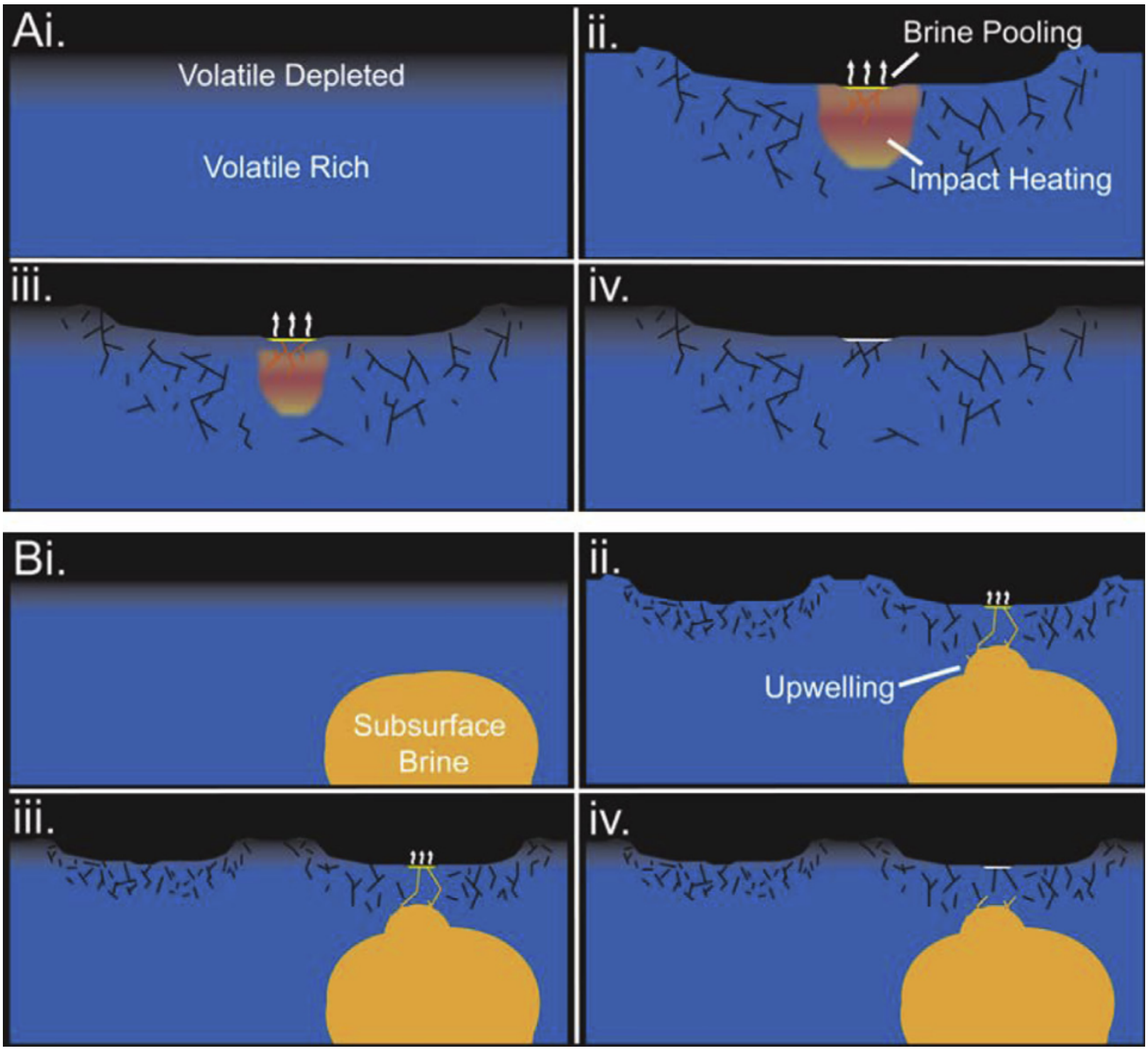

Figure 1.7: Floor bright spot formation mechanisms (Stein et al., 2019).

Ceres' gravity field has a major non-hydrostatic term in the degree 2 sectorial term, which is 3% non-hydrostatic (Ermakov et al., 2017). Ermakov et al. posit several explanations for this observation, among which are a relaxation-resistant viscosity increase at depth due to a compositional boundary, the combination of a bottom buoyant loading from a (frozen in) mantle plume with a rigid lithosphere, and/or salt tectonics (Ermakov et al., 2017). Additionally, Ceres' measured J_2 gravity term is about 10% smaller than expected when assuming that its rotational flattening is hydrostatic, hypothesized by Mao and McKinnon to be caused by either a faster spin rate in the past or a deep-seated uncompensated mass anomaly (X. Mao & McKinnon, 2018).

The presence of convective mantle plumes in Ceres' interior as the cause of the non-hydrostatic gravity term is consistent with theories that cryovolcanic features such as Ahuna Mons are caused by mantle uplifts (Ruesch et al., 2019). Formisano et al. (2020) have proven that thermal convection in the crust is unlikely to occur and will be short-lived if it does. This means that cryovolcanism is most likely driven by diapirism, rather than thermal convection. Nonetheless, mantle uplifts and emplacement of brine reservoirs could still be caused by mantle convection. King et al. (2022) have used a convection model to assess whether radiogenic heating could provide the energy required for the geologic processes observed on Ceres, including the cryovolcanism. They found that for calculations consistent with Ceres, transient, asymmetric convection develops, which can be the cause for the geologic processes observed on Ceres.

Due to the lack of extensive data, there is much that is not clear about Ceres' interior. Much of the research has made assumptions to deal with the underconstrained nature of the problem, and otherwise they produce multiple sets of results to consider multiple possibilities. One of the puzzling features of Ceres' interior is the apparent geologic activity, observed through the evidence of cryovolcanism. Several formation mechanisms of the bright spots are proposed in literature. These differ from each other in the homogeneity of salts in Ceres' crust and the necessity for impact heating in order to bring salty brines to liquid state. This research attempts to determine what the most plausible formation mechanism for the bright spots is. In order to answer this question, interior models and crustal models are developed and verified. This leads to the following set of research questions:

1. What is the formation mechanism of the bright spots on Ceres?
    (a) To what degree is Ceres differentiated?
    (b) How accurate are isostasy-based crust models?
    (c) What are Ceres' crustal properties?
    (d) How correlated are the locations of bright spots and the crustal properties?
    (e) Under which conditions is no external energy source necessary for liquid brine to exist in Ceres' crust?

The insights gleaned from this research will allow for the further establishment of which geologic processes are happening in Ceres' interior. As Ceres is such a unique planetary body, understanding its interior allows us to better understand the nuances of geologic processes in bodies that simultaneously exhibit properties of asteroids, terrestrial planets and icy moons. This would in turn extend our understanding of how planetary bodies form and evolve.

2
Theoretical Framework

This chapter aims to give the reader an overview of the theory and techniques upon which the rest of the work is based, so as to facilitate their understanding of the work.

2.1. Planetary Interiors

The interiors of rocky bodies can be broadly divided into two categories: differentiated and undifferentiated. Rocky bodies are formed from undifferentiated material, in which its constituent components are distributed homogeneously. As a result of internal heating of the body, it can undergo a process called differentiation. In differentiation, components separate based on their density when they are molten. The heavier materials will sink to the bottom, whereas the lighter materials will float to the surface. This process is shown in Figure 2.1. The layers formed in this way are conventionally named the core, mantle and crust. Because this process is heavily dependent on internal heating, and internal heating scales strongly with the size of the body, large bodies are usually at least partially differentiated while smaller bodies have a relatively higher chance to be undifferentiated.

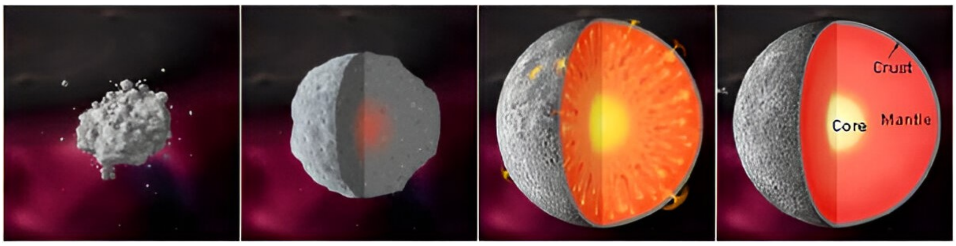

Figure 2.1: Differentiation of a rocky body. Image credits: Smithsonian National Museum of Natural History.

A higher degree of differentiation is usually associated with more flexibility in the material in the upper layers, which leads to a stronger gravitational effect of the equatorial bulge. The Radau-Darwin approximation, which relates the normalized mean moment of inertia I_{norm} to the gravitational effect of the equatorial bulge, J_2 (more on this in the following section), and the ratio of the centrifugal acceleration to the gravitational acceleration q_r, is shown in Equation 2.1. The value of q_r is given by Equation 2.2, in which ω_{rot} is the angular velocity of the body. The Radau-Darwin approximation is valid for bodies that are in hydrostatic equilibrium and are rotating ellipsoids.

$$I_{norm} = \frac{I}{MR^2} \approx \frac{\frac{2}{3}J_2}{J_2 + \frac{1}{3}q_r} \tag{2.1}$$

$$q_r = \frac{\omega_{rot}^2 R^3}{GM} \tag{2.2}$$

The moment of inertia of a body is a good measure for the degree of differentiation of a body, because it is essentially a measure of how much mass of the body is situated far away from its center, as evident from its definition (Equation 2.3). Additionally, the more differentiated a body is, the more its mass is concentrated at its center.

$$I = \int_m r^2 dm \tag{2.3}$$

Given a density profile of the interior of a planet, the internal pressure can be calculated using the system of equations given by Equation 2.4, 2.5 and 2.6, where r is the distance from the center of Ceres, G is the gravitational constant, M is the mass, g is the gravitational acceleration, ρ is the density and p is the pressure.

$$dp = -\rho(r)g(r)dr \tag{2.4}$$

$$dM = 4\pi\rho(r)r^2 dr \tag{2.5}$$

$$g(r) = \frac{GM(r)}{r^2} \tag{2.6}$$

In order to calculate a profile from these equations, the first two must be numerically integrated. In this work, this is done using an Euler integrator with a step size Δr of 1 m, for which the resulting iterative equations, moving from one point to the next, are given in Equation 2.7 and 2.8.

$$p_{n+1} = p_n + \left.\frac{dp}{dr}\right|_n \Delta r \tag{2.7}$$

$$M_{n+1} = M_n + \left.\frac{dM}{dr}\right|_n \Delta r \tag{2.8}$$

It is important to note that first the mass of the planet is integrated upwards, starting from 0 at the center of the body to the planetary mass M at the surface. Then, the pressure is integrated downwards, from 0 at the surface of the body to the maximum pressure at its center.

2.2. Spherical Harmonics

Spherical harmonics are a widely used way to represent gravity potential fields of planets, but they can also be used to represent other types of fields on the surfaces of spheres, such as the terrain height, crust thickness or crust density of a planet. For the gravitational potential U of a planet, the spherical harmonic representation is given by Equation 2.9. In this equation, r is the distance from the center of the planet, θ is the latitude, λ is the longitude, G is the gravitational constant, M is the planetary mass and R is the planetary radius. The variable n is called the degree, and m the order. Each combination of degree and order has an associated fully normalized Legendre polynomial $\bar{P}_{nm}$ and two (normalized) coefficients, $\bar{C}_{nm}$ and $\bar{S}_{nm}$.

$$U(r,\theta,\lambda) = \frac{GM}{R}\sum_{n=0}^{\infty}\left(\frac{R}{r}\right)^{n+1}\sum_{m=0}^{n}\bar{P}_{nm}(\sin\theta)(\bar{C}_{nm}\cos m\lambda + \bar{S}_{nm}\sin m\lambda) \tag{2.9}$$

The combination of degree and order determine the shape, projected on a sphere of radius R, of a term in the summation, and the coefficients determine the strength of that shape. By summing each combination, the full potential field of the planet is found, and so the complete field can be represented by the combination of all the coefficients. The shapes of the first few degrees and orders are shown in Figure 2.2. The terms where the order is zero are called zonal terms, as they form horizontal bands across the planet. The terms where the order is equal to the degree are called sectorial terms, and they form vertical bands across the planet. The remaining terms are called tesseral. The degree zero term is special in that it represents the point mass gravity of the planet, and when the coefficients are normalized to this value, the coefficient $\bar{C}_{00}$ is always equal to 1.

Relevant to this work are the hydrostatic zonal coefficients $\bar{C}_{20}$ and $\bar{C}_{40}$, because they are related to the deformation of a planet due to its rotation. Analogous coefficients for a different representation of spherical harmonics are often used, and are called J_2 and J_4, respectively, where $J_2 = -C_{20}$ and $J_4 = -C_{40}$.

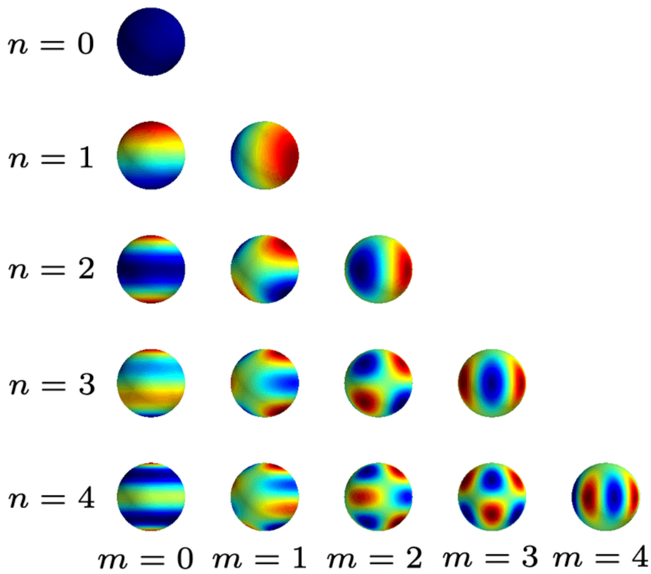

Figure 2.2: Visualization of the shape of the first few spherical harmonics terms (Hollebon & Fazi, 2020).

2.3. Crust Modelling

In a homogeneous body, the gravity signal is highly correlated with the topography. To investigate this correlation, one can subtract the expected gravity field from topography with a constant density from the measured gravity field. This process is called a Bouguer correction, and the remaining gravity anomaly is called the Bouguer anomaly. Since gravitational acceleration is proportional to the attracting mass, it is expected that a stronger acceleration would be experienced when overhead of higher terrain (more mass), and a weaker acceleration when overhead of lower terrain (less mass). Therefore, a simple Bouguer correction is given by Equation 2.10, in which δg_B is the expected gravity from the topography, ρ_c is the density of the crust material, and h is the terrain height.

$$\delta g_B = 2\pi G \rho_c h \tag{2.10}$$

A significant Bouguer anomaly indicates that a crust with constant depth and density is too simplistic of a model. More sophisticated models are based on the concept of isostasy, in which it is assumed the crust essentially floats on top of the mantle. Isostatic equilibrium implies that the crust has had time to settle and that there are no lateral gradients in pressure, so that there is no flow taking place and the interior is in equilibrium. For a crust with surface topography, isostatic equilibrium can only be achieved if the topography is compensated for in the interior.

Two models for isostatic compensation are Pratt compensation and Airy compensation, in which the topography is compensated by the density of the crust layer, and the depth of the crust layer, respectively. These models are shown diagrammatically in Figure 2.3. In the Pratt model, the crust underneath high topography is lighter than that underneath low topography, so that the pressure underneath both remains the same. In the Airy model, the crust is thicker underneath high topography than underneath low topography, so that more of the heavier mantle material is displaced, meaning that there is more buoyancy force to support the topography.

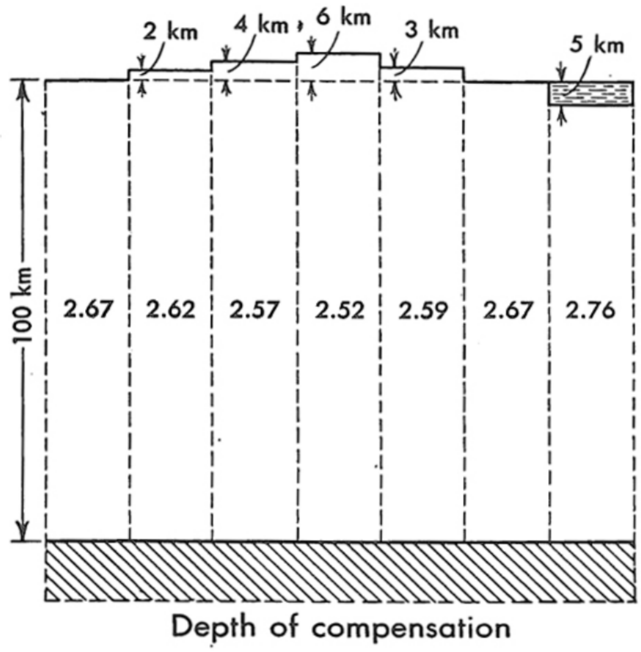

(a) Pratt compensation.

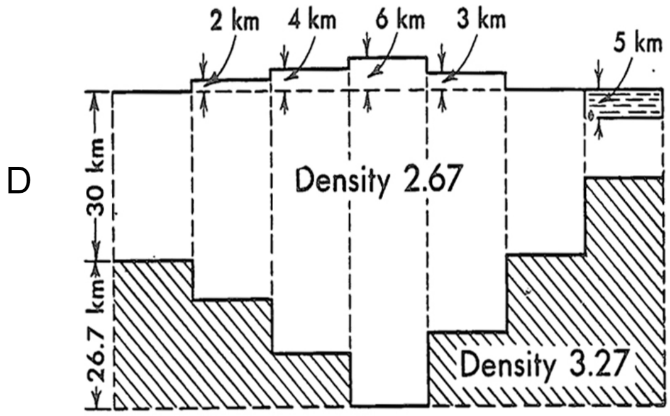

(b) Airy compensation.

Figure 2.3: Different kinds of local isostatic compensation (Heiskanen & Vening Meinesz, 1959).

The density at an arbitrary location of the crust in the Pratt model is given by Equation 2.11, where ρ_c is the local crust density, ρ_{ref} is the reference density, T_{ref} is the reference thickness, and h_t is the local topography height. The reference values are chosen to correspond with a topography height of zero.

$$\rho_c = \rho_{ref} \frac{T_{ref}}{T_{ref} + h_t} \tag{2.11}$$

For Airy compensation, there are multiple ways to calculate the crust thickness. Traditionally, the deviation of the lower boundary of the crust from the reference depth is calculated using the equal masses approach, which assumes a uniform gravitational field. This assumption leads to a small error if the crust thickness is a very small fraction of the radius of the body, such as in the case of the Earth. However, for smaller bodies, such as Ceres, this can lead to a significant error, in which case one would like to opt for the equal pressures approach. This approach does not use the assumption on the gravity field, but is therefore a bit more complicated. The formulas used to calculate the deviation from the reference depth are taken from Hemingway and Matsuyama (2017), and are shown in Equation 2.12

and Equation 2.13 for the equal masses and equal pressures method, respectively. In these equations, h_b is the deviation from the reference depth (positive downwards), h_t is the topography of the surface of the crust, ρ_c is the density of the crustal material, $\Delta\rho$ is the density contrast between the crust and mantle, g_t is the gravitational acceleration at the top of the crust, and g_b is the gravitational acceleration at the bottom of the crust.

$$h_b = h_t \frac{\rho_c}{\Delta\rho} \tag{2.12}$$

$$h_b = h_t \frac{\rho_c}{\Delta\rho} \frac{g_t}{g_b} \tag{2.13}$$

These models implicitly assume local isostasy, where every feature of topography is compensated only by the crust directly underneath it. An extension of these models are flexure models, which assume that topography features are supported by an elastic lithosphere, which deflects to support the weight of the feature. This is called regional isostasy, and the difference between local and regional isostasy is visualized in Figure 2.4.

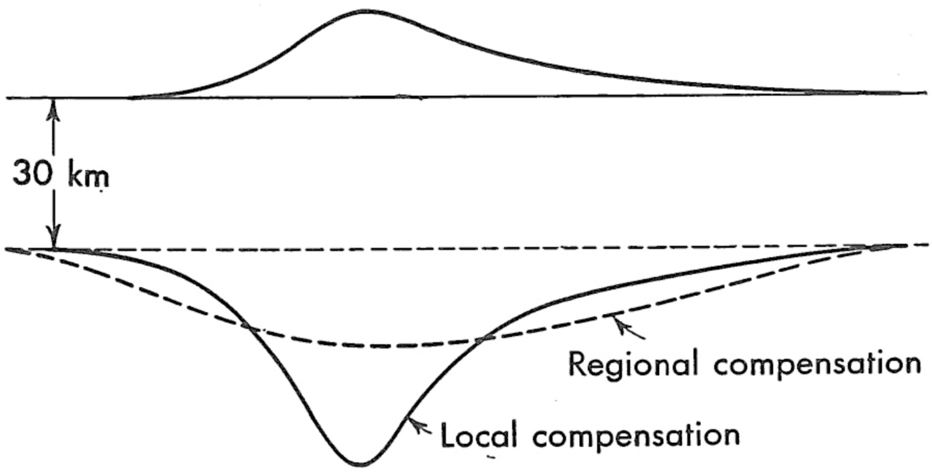

Figure 2.4: Difference between local and regional isostasy (Heiskanen & Vening Meinesz, 1959).

Regional isostasy is modelled by the flexural response function, which calculates for each spherical harmonic degree of the crust thickness by which value between 0 and 1 it should be multiplied, depending on the mechanical properties of the elastic lithosphere. The low degrees are always kept at 100%, and the very highest degrees are always set to 0, but where and how fast this transition occurs is what is calculated by the flexural response function. Therefore, what the flexure model essentially does is smooth out the changes in crust depth by keeping only the low degrees of the spherical harmonics of the crust thickness. The flexural response function of an infinite plate is given by Equation 2.14, where n is the spherical harmonic degree, D is the flexural rigidity of the lithosphere, ρ_m is the density of the mantle, and R is the radius of the planet. The flexural rigidity is given by Equation 2.15, where E is the Young's modulus of the lithosphere material, T_e is the elastic lithosphere thickness, and ν is the lithosphere material's Poisson ratio. For small planets, the approximation of the crust as an infinite plate leads to significant errors. For those, the flexural response function is calculated for a thin shell, as given in Equation 2.16.

$$\Phi(n) = \left(1 + \frac{D}{(\rho_m - \rho_c)g_t}\left(\frac{2(n+1)}{2R}\right)^4\right)^{-1} \tag{2.14}$$

$$D = \frac{ET_e^3}{12(1-\nu^2)} \tag{2.15}$$

$$\Phi(n) = \left(1 + \frac{D}{(\rho_m - \rho_c)g_t}\left(\frac{1}{R^4}\frac{\left(n(n+1)-2\right)^2}{1-\frac{1-\nu}{n(n+1)}} + \frac{12(1-\nu^2)}{T_e^2 R^2}\frac{1-\frac{2}{n(n+1)}}{1-\frac{1-\nu}{n(n+1)}}\right)\right)^{-1} \tag{2.16}$$

These are all the equations necessary for the creation of crust models.

3

Interior Modelling

The first step to understanding Ceres' interior is to develop models of its structure, crust and temperature. The structure and temperature of the entire interior of the dwarf planet are described using spherically symmetric density and temperature profiles, respectively. Crust models can produce laterally varying models for the top layer, on the other hand. This chapter describes the methods used to obtain these models.

3.1. Data

Measurements of Ceres that are useful to constrain its structure are limited to its mass, moment of inertia, shape, and gravity field. Ceres' mass is taken to be $9.3834 \cdot 10^{20}$ kg (Konopliv et al., 2018), and its normalized moment of inertia is taken to be 0.375 (X. Mao & McKinnon, 2018).

The topography dataset used is from a digital terrain model resulting from a stereo photogrammetry study by the German Aerospace Center [1], and it is shown in Figure 3.1. This figure shows the topography of Ceres with respect to the reference ellipsoid (which is obtained by setting C_{00} and C_{20} to zero). The topography ranges from -6 km to 8 km with notable high points in the north pole and notable low points in the east.

The gravity field is obtained by using the spherical harmonics coefficients in the Ceres18C dataset developed by Konopliv et al. (2018). The gravity field, with the major hydrostatic terms J2 and J4 set to 0, is shown in Figure 3.2. Here it is shown that the residual acceleration is between -230 and 220 mGal.

[1] https://astrogeology.usgs.gov/search/map/ceres_dawn_fc2_hamo_global_dtm_137m, retrieved June 5th 2024

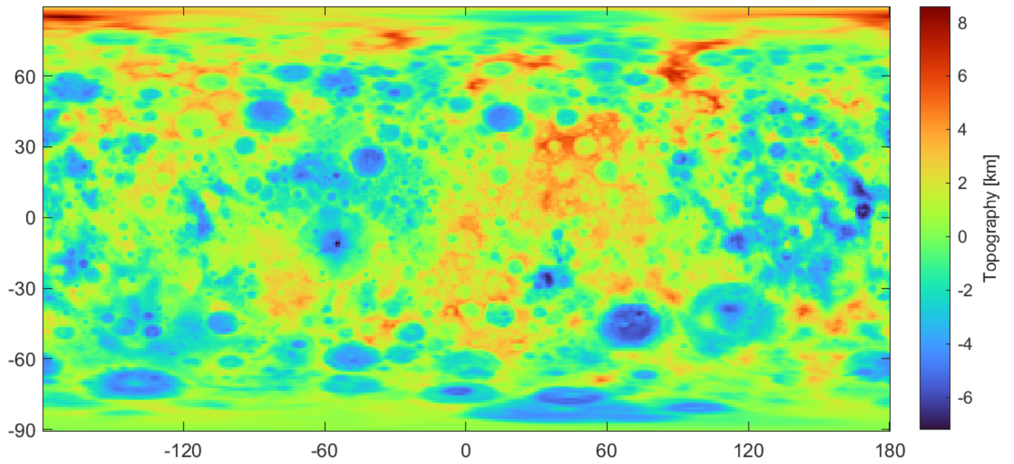

Figure 3.1: Ceres' topography (DLR, n.d.).

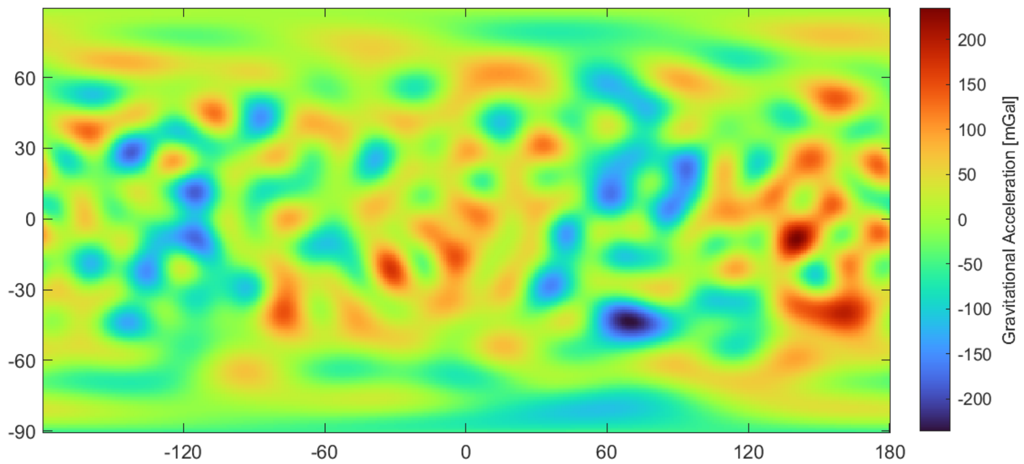

Figure 3.2: Ceres' gravity field (Konopliv et al., 2018). The major hydrostatic terms J2 and J4 are set to 0.

Figure 3.1 and Figure 3.2 both show a vertical banded pattern that is almost inverted, but not quite. This lack of correlation is especially clear when looking at the area around longitude 0, where the topography is part of the highlands slightly east, but the gravity is part of the stronger are slightly west.

3.2. Spherically Symmetric Density Profiles

The normalized moment of inertia of a planet is calculated using Equation 3.1, where I is the measured moment of inertia, M is the mass of the planet, and R is the radius of the planet. For a homogeneous sphere, as its moment of inertia is given by $I = 0.4MR^2$, the normalized moment of inertia is 0.4. Ceres' normalized moment of inertia being smaller than this value implies a mass concentration closer to the center.

$$I_{norm} = \frac{I}{MR^2} \tag{3.1}$$

A density profile that would explain this mass concentration can be constrained using the mass and moment of inertia. For an arbitrary density profile, as a function of the distance r from the center of the body, $\rho(r)$, the mass and moment of inertia of the body are given by Equation 3.2 and Equation 3.3, respectively. Setting the incremental change in volume dV equal to the volume of a plate with incremental thickness dr and area equal to the surface area of a sphere with radius r yields Equation 3.4. Substituting this equation into Equation 3.2 and Equation 3.3 yields Equation 3.5 and Equation 3.6, respectively. These equations can be validated by substituting a constant value ρ for $\rho(r)$ and performing the integration to obtain the familiar formulas for the mass and mass moment of inertia for a homogeneous sphere.

$$M = \int_m dm = \int_V \rho(r) dV \tag{3.2}$$

$$I = \int_m r^2 dm = \int_V r^2 \rho(r) dV \tag{3.3}$$

$$dV = 4\pi r^2 dr \tag{3.4}$$

$$M = 4\pi \int_0^R r^2 \rho(r) dr \tag{3.5}$$

$$I = 4\pi \int_0^R r^4 \rho(r) dr \tag{3.6}$$

The simplest density profile that can explain the mass concentration is a linear one, given by $\rho(r) = c_0 + c_1 r$, where c_0 and c_1 are arbitrary constants. Substituting this into Equation 3.5 and Equation 3.6 and evaluating the integrals results in a system of equations given by Equation 3.7. This system can be solved uniquely, because the linear density profile has two unknowns and there are 2 constraints. A quadratic profile, given by $\rho(r) = c_0 + c_1 r + c_2 r^2$, has one additional constraint, and so results in a family of solutions. If c_0 (effectively the core density) is taken as the free variable, the remaining two constants can be calculated using Equation 3.8. The same thing can be done for a cubic profile, $\rho(r) = c_0 + c_1 r + c_2 r^2 + c_3 r^3$, by assuming that the first derivative of the profile is 0 at the core of the planet, which leads to $c_1 = 0$. The remaining two constants can then be calculated using Equation 3.9.

$$\begin{bmatrix} \frac{M}{4\pi R^3} \\ \frac{I}{4\pi R^5} \end{bmatrix} = \begin{bmatrix} \frac{1}{3} & \frac{R}{4} \\ \frac{1}{5} & \frac{R}{6} \end{bmatrix} \begin{bmatrix} c_0 \\ c_1 \end{bmatrix} \tag{3.7}$$

$$\begin{bmatrix} \frac{M}{4\pi R^3} - \frac{c_0}{3} \\ \frac{I}{4\pi R^5} - \frac{c_0}{5} \end{bmatrix} = \begin{bmatrix} \frac{R}{4} & \frac{R^2}{5} \\ \frac{R}{6} & \frac{R^2}{7} \end{bmatrix} \begin{bmatrix} c_1 \\ c_2 \end{bmatrix} \tag{3.8}$$

$$\begin{bmatrix} \frac{M}{4\pi R^3} - \frac{c_0}{3} \\ \frac{I}{4\pi R^5} - \frac{c_0}{5} \end{bmatrix} = \begin{bmatrix} \frac{R^2}{5} & \frac{R^3}{6} \\ \frac{R^2}{7} & \frac{R^3}{8} \end{bmatrix} \begin{bmatrix} c_2 \\ c_3 \end{bmatrix} \tag{3.9}$$

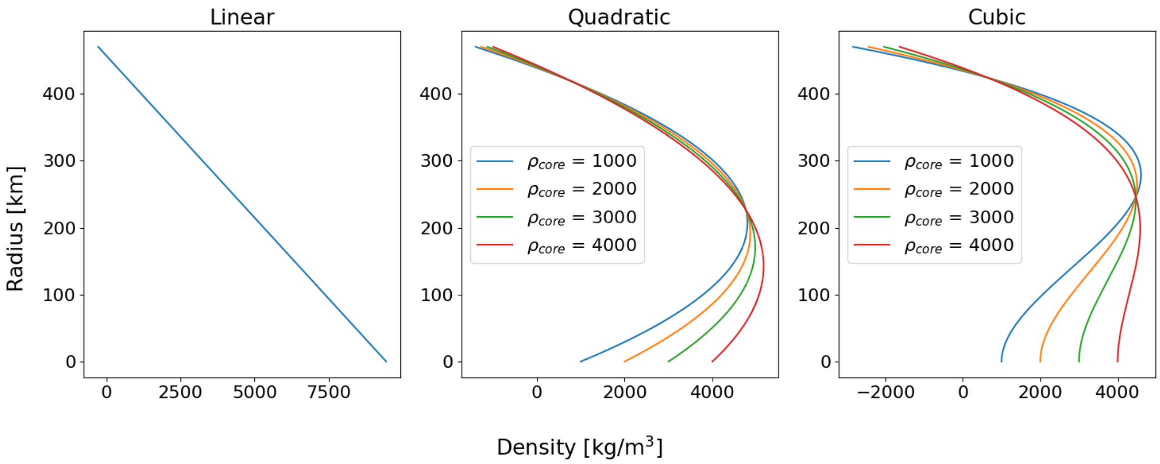

Figure 3.3: Polynomial density profiles constrained my the mass and moment of inertia.

The density profiles that follow from these calculations are shown in Figure 3.3, in which it is clear that these solutions are not realistic, as they contain negative densities, and higher densities on top of lower densities. Finally, to investigate the suitability of polynomial density profiles, a 7th order polynomial model ($\rho(r) = c_0 + c_1 r + c_2 r^2 + c_3 r^3 + c_4 r^4 + c_5 r^5 + c_6 r^6 + c_7 r^7$) is created by assuming the first and second derivatives of the profile are 0 at the domain boundaries ($r = 0$ and $r = R$), and that the core density is that of iron ($\rho(0) = c_0 = 7900$ kg/m^3) and the outermost density is that of ice ($\rho(R) = c_8 = 910$ kg/m^3), corresponding to the most extreme case. This leads to the system in Equation 3.10, where the first two rows correspond to the requirements of the derivatives at $r = R$, the third row corresponds to the requirement on the outer density, and the last two rows correspond to the mass and moment of inertia constraints. This leads to the model shown in Figure 3.4, where it is visible that there is still some unrealistic overshoot at the boundaries. The conclusion that can be drawn from this is that the change in density happens more suddenly than the smooth polynomial models can accommodate. Therefore, models with more sudden, or even discontinuous, density changes must be considered.

$$\begin{bmatrix} 0 \\ 0 \\ c_8 - c_0 \\ \frac{M}{4\pi R^3} - \frac{c_0}{3} \\ \frac{I}{4\pi R^5} - \frac{c_0}{5} \end{bmatrix} = \begin{bmatrix} 3 & 4R & 5R^2 & 6R^3 & 7R^4 \\ 6 & 12R & 20R^2 & 30R^3 & 42R^4 \\ R^3 & R^4 & R^5 & R^6 & R^7 \\ \frac{R^3}{6} & \frac{R^4}{7} & \frac{R^5}{8} & \frac{R^6}{9} & \frac{R^7}{10} \\ \frac{R^3}{8} & \frac{R^4}{9} & \frac{R^5}{10} & \frac{R^6}{11} & \frac{R^7}{12} \end{bmatrix} \begin{bmatrix} c_3 \\ c_4 \\ c_5 \\ c_6 \\ c_7 \end{bmatrix} \tag{3.10}$$

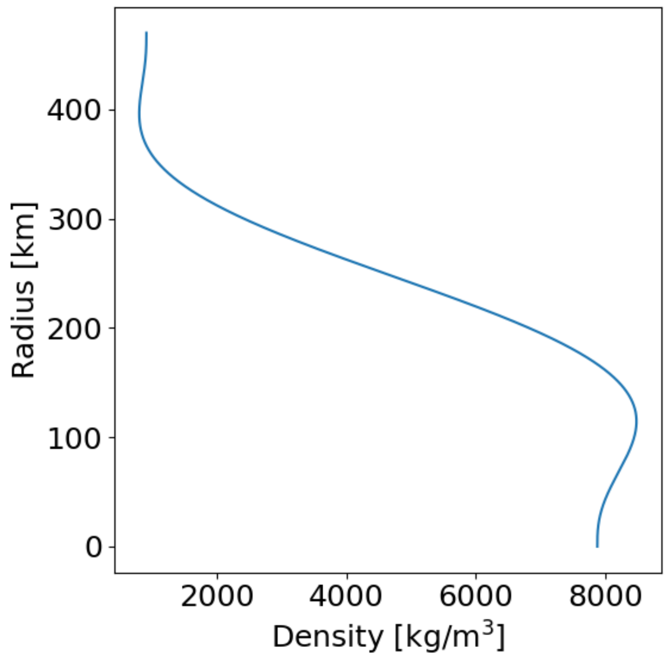

Figure 3.4: 7th order polynomial density profile.

Models with discontinuous density changes are those with discrete layers of different densities. The most parsimonious layered model is one with two layers, called the mantle and the crust in this work. This model has three unknowns, the mantle density ρ_m, the crust density ρ_c and the boundary radius r_{bound}. Given the formulas for the mass of a homogeneous sphere (Equation 3.11) and the moment of inertia of a homogeneous sphere (Equation 3.12), the mass and moment of inertia of a two-layer planet are given by Equation 3.13 and Equation 3.14, respectively.

$$M = \rho V = \frac{4}{3}\pi\rho R^3 \tag{3.11}$$

$$I = \frac{2}{5}MR^2 = \frac{8}{15}\pi\rho R^5 \tag{3.12}$$

$$M = \frac{4}{3}\pi\left(r_{bound}^3\rho_m + (R^3 - r_{bound}^3)\rho_c\right) \tag{3.13}$$

$$I = \frac{8}{15}\pi\left(r_{bound}^5\rho_m + (R^5 - r_{bound}^5)\rho_c\right) \tag{3.14}$$

When r_{bound} is taken as the free variable, Equation 3.13 and Equation 3.14 form a system of equations that is linear in ρ_m and ρ_c, shown in Equation 3.15. This system forms a family of solutions where every value of the boundary radius corresponds to a combination of mantle and crust density that meet both the mass and the moment of inertia requirements. This family of solutions is shown in Figure 3.5.

$$\begin{bmatrix} \frac{3M}{4\pi} \\ \frac{15I}{8\pi} \end{bmatrix} = \begin{bmatrix} r_{bound}^3 & R^3 - r_{bound}^3 \\ r_{bound}^5 & R^5 - r_{bound}^5 \end{bmatrix} \begin{bmatrix} \rho_m \\ \rho_c \end{bmatrix} \tag{3.15}$$

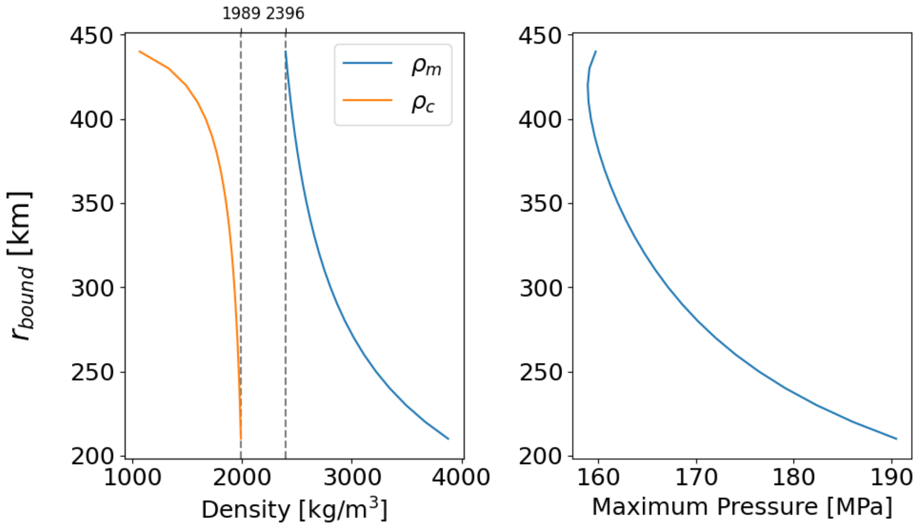

Figure 3.5: 2 layer solutions for the interior structure that meet the mass and moment of inertia requirements. The maximum internal pressure (which is found at the core) is shown for every solution. Only the solutions that satisfy $\rho_c > 900$ kg/m^3 and $\rho_m < 4000$ kg/m^3 are considered, leading to a maximum bound 1989 kg/m^3 on ρ_c and a minimum bound of 2396 kg/m^3 on ρ_m.

On the left side of Figure 3.5, the mantle and crust densities are shown as a function of the boundary radius. Only the solutions where the crust density is more than that of water ice and the mantle density is less than 4000 kg/m^3 are considered, roughly consistent with the maximum density of silicates. This constraint leads to a maximum crust density of 1989 kg/m^3 and a minimum mantle density of 2396 kg/m^3. The right side of the figure shows the maximum pressure of each of these solutions, where it can be seen that the maximum pressure does not exceed 200 MPa.

In order to assess whether a model with a constant density in each layer is realistic, the equation of state, given in Equation 3.16, is considered. In the equation of state, ρ_0 signifies the nominal density of the material, before its temperature is changed or it's pressurized, α_T is the thermal expansion coefficient of the material, ΔT is the difference in temperature from the nominal case, K is the bulk modulus of the material, and Δp is the difference in pressure from the nominal case.

$$\rho = \rho_0(1 - \alpha_T \Delta T + \frac{1}{K}\Delta p) \tag{3.16}$$

The worst-case-scenario is considered, so that there can be high confidence that the effect of temperature and pressure on the density is negligible. The highest expected thermal expansion coefficient corresponds to a metal or ceramic and is less than 10^{-4} K^{-1} (Ashby et al., 2014), and the highest expected temperature in Ceres' interior is 500 K (Neumann et al., 2020), leading to a change in density of 5%. The lowest expected bulk modulus corresponds to water ice and is 8.4 GPa (Neumeier, 2018), using the previously found maximum expected pressure of 200 MPa leads to a change in density of 2.38%.

Two conclusions can be drawn from this. The first is that the change in density due to temperature and pressure are small enough that ignoring them will not introduce significant error. The second is that any significant change in density in Ceres' material, which must exist considering its moment of inertia, is purely due to a change in composition.

An unsuccessful attempt was made to constrain the composition of Ceres to the known atomic proportions of terrestrial bodies from McDonough and Yoshizaki (2021), shown in Figure 3.6. The attempt was not successful due to the high amount of water (and therefore hydrogen) on Ceres, which is not consistent with other terrestrial bodies. This problem seemingly supports theories that Ceres formed further out in the solar system.

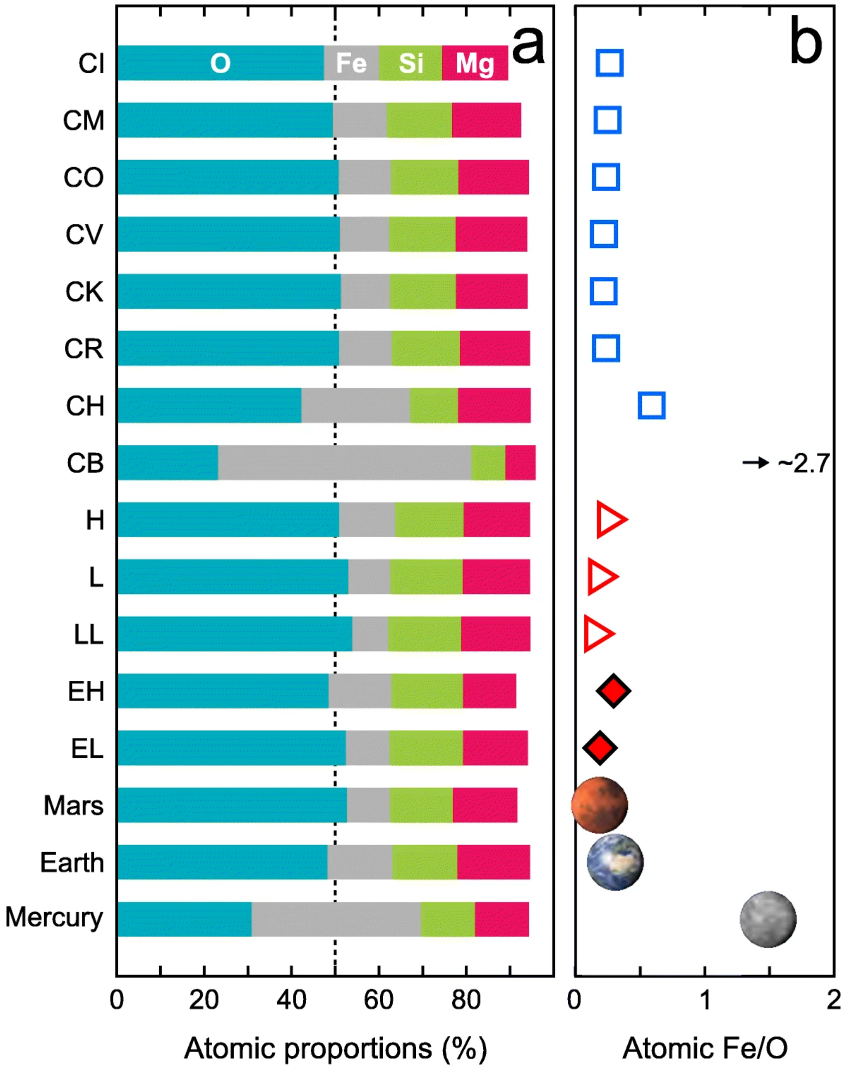

Figure 3.6: Atomic proportions of terrestrial bodies (McDonough & Yoshizaki, 2021).

The structure is further constrained by using the gravity field, coupling the inputs to the 1D structure model and crust models to find the inputs that formed the best performing crust models.

3.3. Crust Models

Two crust models are considered: an Airy compensated crust and a Pratt compensated crust. The inputs to the Airy crust are the reference depth, the mantle density and the crust density. The reference depth, the thickness of the crust when there is no topography, is analogous to the planetary radius minus the boundary radius in the 1D structure model and so can be related one-to-one to the boundary radius. This means the 1D structure model and the Airy crust model have the same inputs. The Pratt model has two inputs, the compensation depth and the reference density. If the compensation depth is interpreted as the crust thickness, that is, the crust is interpreted to be the part of the planet that supports the topography, and the reference density is interpreted as the nominal crust density, the inputs to the Pratt model can also be related to the inputs of the 1D structure model.

The values of the inputs that lead to the best performing model are determined by calculating the root-mean-square-error of the resulting model's degree variance spectrum to that of the measured gravity field. The degree variance of the measured gravity field is shown in Figure 3.7.

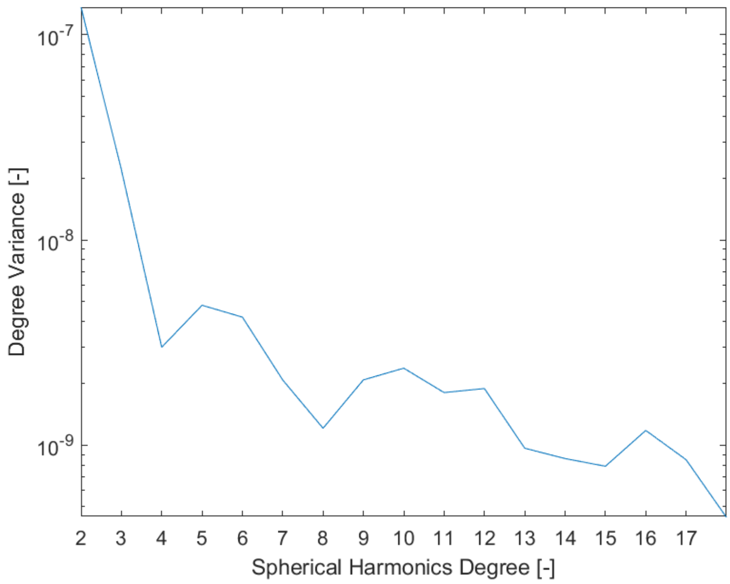

Figure 3.7: Degree variance spectrum of the measured gravity field (Konopliv et al., 2018).

By visual inspection, it is determined that the greatest correlation between the shapes of the gravity fields from measurments and models is found for the spherical harmonic degrees 5-14, as shown in Figure 3.8. Therefore, the models are only optimized to fit the degree variance for degrees 5-14.

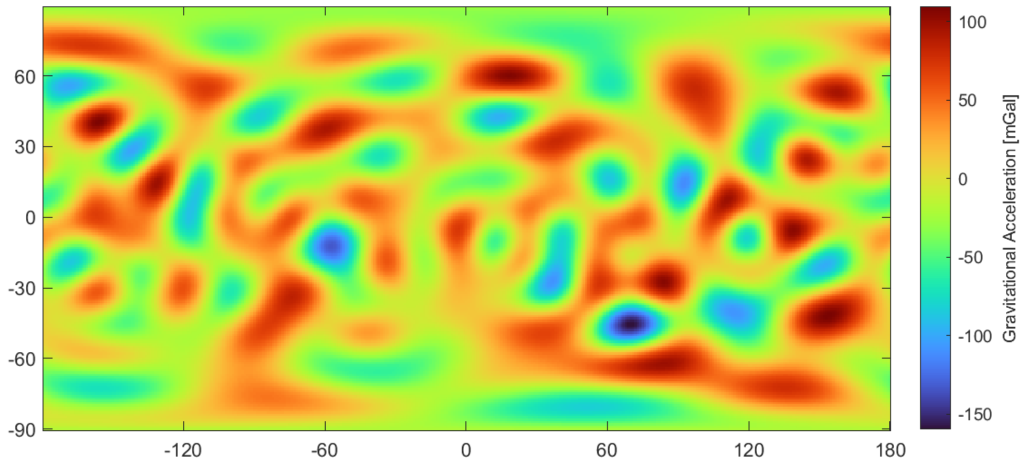

(a) Measured gravity field.

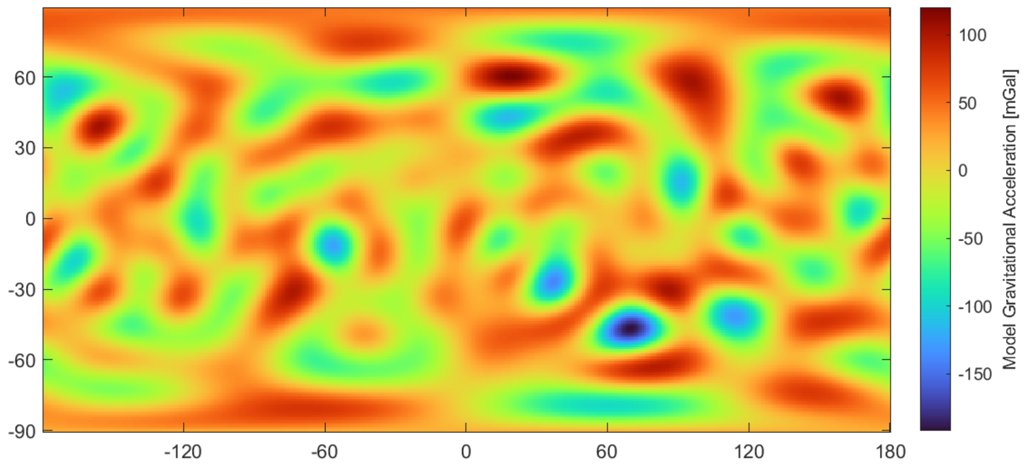

(b) Modelled gravity field.

Figure 3.8: Gravity fields from measurements and crust modelling for spherical harmonic degrees 5-14. The modelled crust is from a Pratt model, but the shape is the same for an Airy model.

Sensitivity analyses are performed for the input variables of the Airy and Pratt models. The results for the Airy model are shown in Figure 3.9. In Figure 3.9a, it is seen that the difference in power between the degrees become more pronounced with a higher value of the reference depth, and the effect of increasing the reference depth decreases the higher it is. Figure 3.9b shows that the mantle density doesn't affect the low degrees as strongly as the high degrees, and that the power spectrum quite quickly converges with increasing mantle density. The effect of the crust density, as shown in Figure 3.9c, is seen to become unstable for high values because it gets close to the mantle density, which invalidates the model.

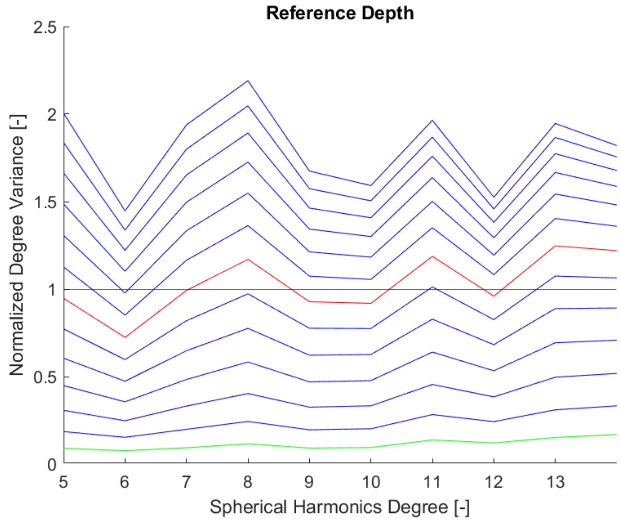

(a) Sensitivity analysis of the reference depth. Values were varied between 10 km and 70 km in steps of 5 km.

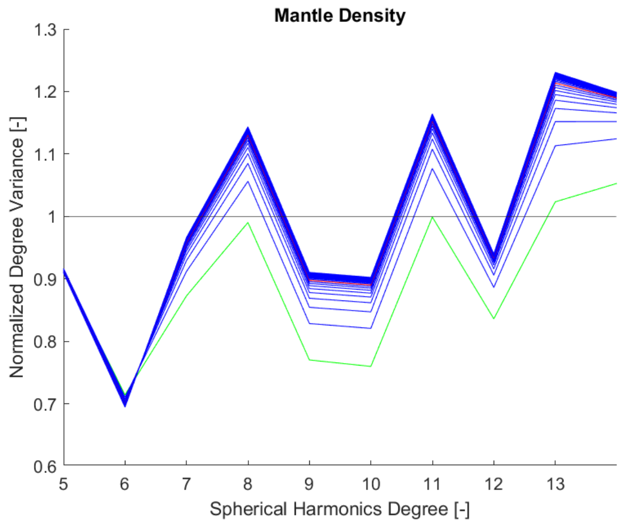

(b) Sensitivity analysis of the mantle density. Values were varied between 1500 kg/m^3 and 4000 kg/m^3 in steps of 100 kg/m^3.

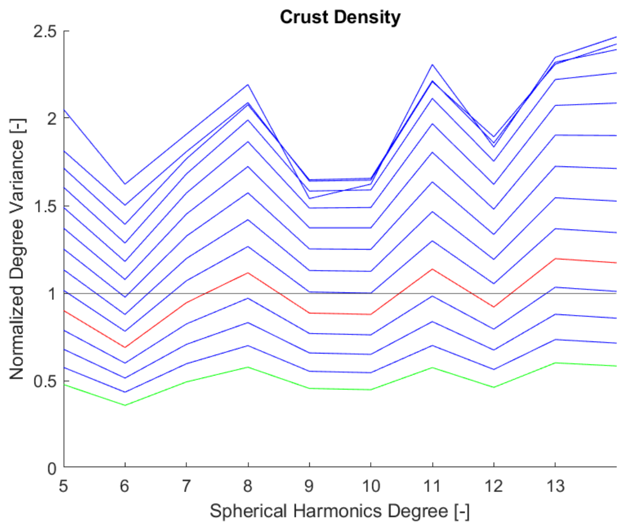

(c) Sensitivity analysis of the crust density. Values were varied between 900 kg/m^3 and 2200 kg/m^3 in steps of 100 kg/m^3.

Figure 3.9: Sensitivity analysis for input variables of the Airy model, showing the degree variance spectrum of the modelled gravity field normalized by the degree variance of the measured gravity field. The green line indicates the lowest value for the variable, whereas the red line indicates the nominal model. The nominal model has a reference depth of 39 km, a crust density of 1310 kg/m^3 and a mantle density of 2410 kg/m^3.

The sensitivity analysis for the Pratt model is shown in Figure 3.10. Figure 3.10a indicates that the lower degrees are more affected by the compensation depth than the higher degrees, and the effect of increasing the compensation depth decreases with increasing the compensation depth. It can be noted from Figure 3.10b that the higher degrees are more affected by the reference density than the low degrees, and that the effect of increasing the reference density actually increases with increasing reference density.

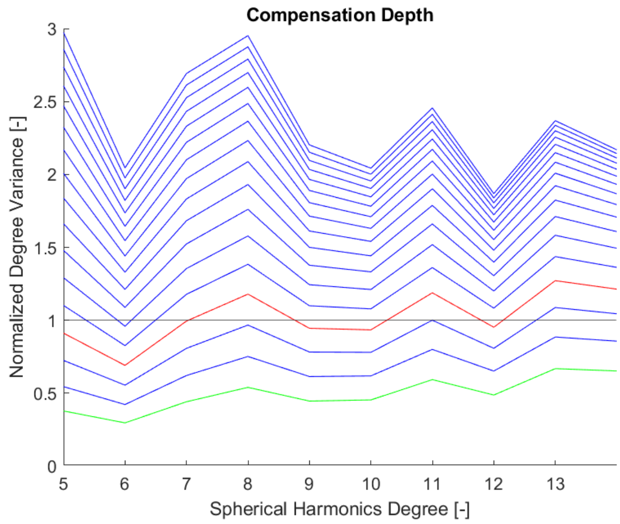

(a) Sensitivity analysis of the compensation depth. Values were varied between 40 km and 200 km in steps of 10 km.

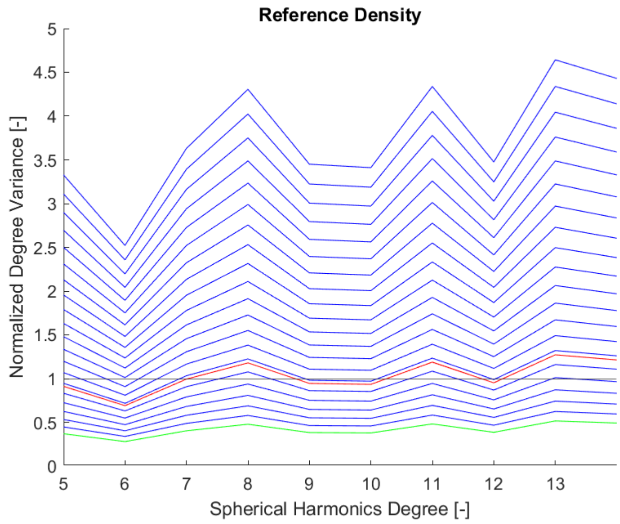

(b) Sensitivity analysis of the reference density. Values were varied between 1000 kg/m^3 and 3000 kg/m^3 in steps of 100 kg/m^3.

Figure 3.10: Sensitivity analysis for input variables of the Pratt model, showing the degree variance spectrum of the modelled gravity field normalized by the degree variance of the measured gravity field. The green line indicates the lowest value for the variable, whereas the red line indicates the nominal model. The nominal model has a compensation depth of 70 km and a reference density of 1570 kg/m^3.

To find the optimal Airy model, every reference depth between 30 km and 50 km is evaluated in steps of 1 km. For each of these reference depths, the corresponding mantle and crust densities are determined using Equation 3.15. The Airy crust model is then created and its degree variance calculated. Its performance is measured using the root-mean-square-error of this degree variance spectrum to that of the measured gravity field. The results of this procedure are shown in Figure 3.11, and there is clearly a minimum between 39 km and 40 km. Out of the tried values, 39 km had the absolute lowest root-mean-square-error, where the mantle density is 2410 kg/m^3 and the crust density is 1310 kg/m^3.

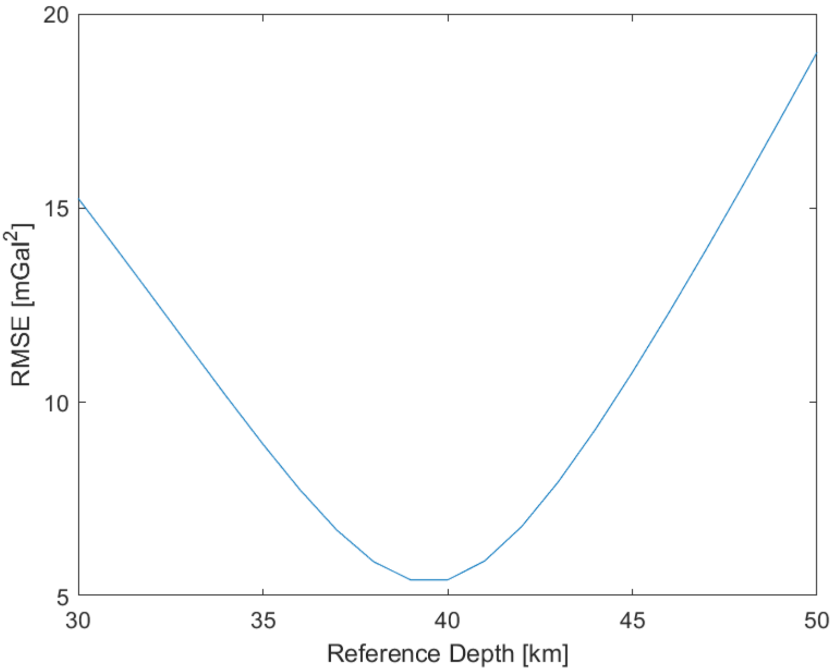

Figure 3.11: Root-mean-square-error of Airy models with different reference depths. The mantle and crust densities for the models are determined using Equation 3.15.

A simple grid search is performed to determine the optimal Pratt model, where the compensation depth is varied between 50 km and 80 km in steps of 1 km, and the reference density is changed between 1500 kg/m^3 and 1800 kg/m^3 in steps of 10 kg/m^3. The results are shown in Figure 3.12. In Figure 3.12a it is visible that there are many combinations where the inputs are adjusted to each other to produce a low error. This is even more clear in Figure 3.12b, where the yellow squares indicate solutions that perform only a couple of percents worse than the best solution. Therefore, a solution in this area can be chosen where the compensation depth and reference density correspond to a combination of layer boundary radius and crust density that meets the mass and moment of inertia requirements. This solution is found to be at a compensation depth of 70 km and a reference density of 1570 kg/m^3, which leads to a mantle density of 2520 kg/m^3.

The selected crust models are shown in Figure 3.13. Of course, the shape of these models in directly related to the topography. In the Airy model shown in Figure 3.13a, the crust thickness varies between 24 km and 57 km, whereas in the Pratt model shown in Figure 3.13b, the crust density varies between 1400 kg/m^3 and 1750 kg/m^3. These densities indicate significant rock content in the crust, because they are all much higher than the density of ice.

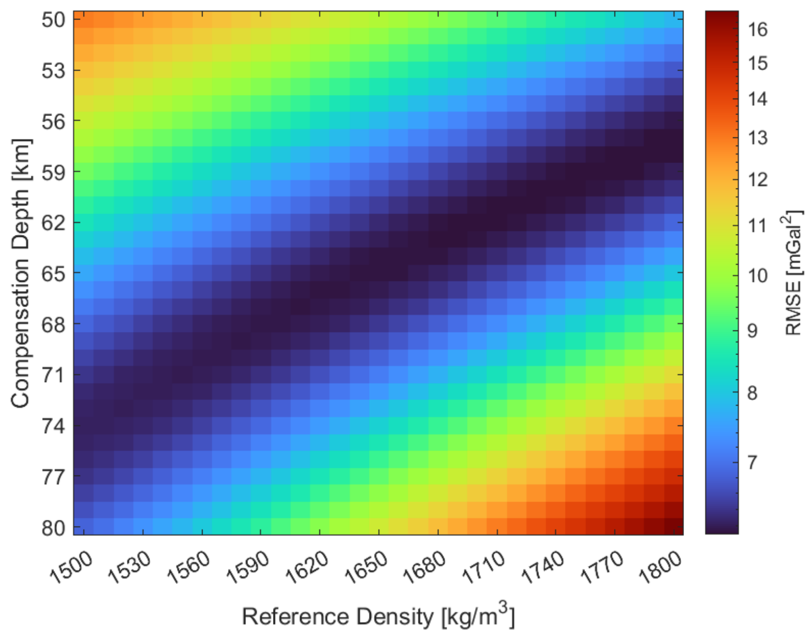

(a) The root-mean-square-error of the grid search.

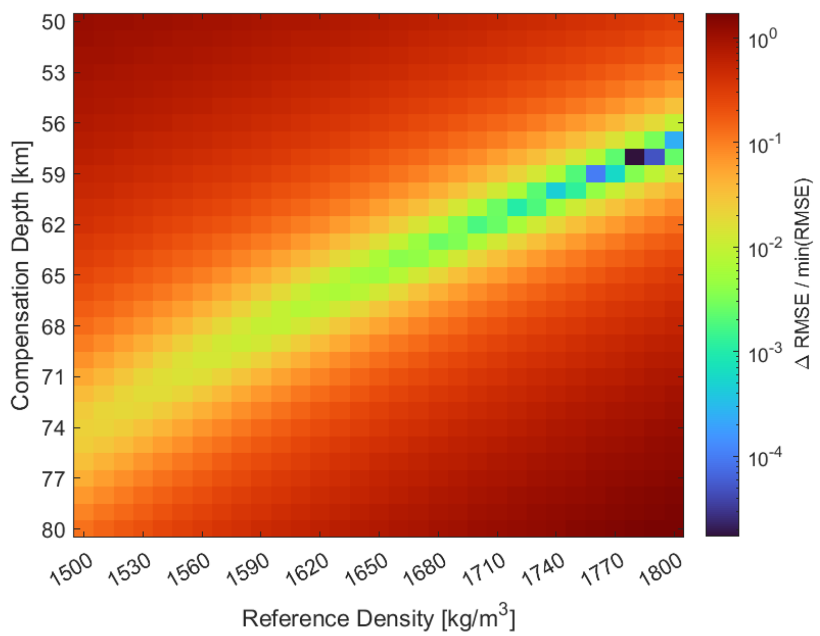

(b) The difference of the root-mean-square-error of each model with respect to the lowest value, normalized by the same value.

Figure 3.12: Results of the grid search for the optimal Pratt inputs values.

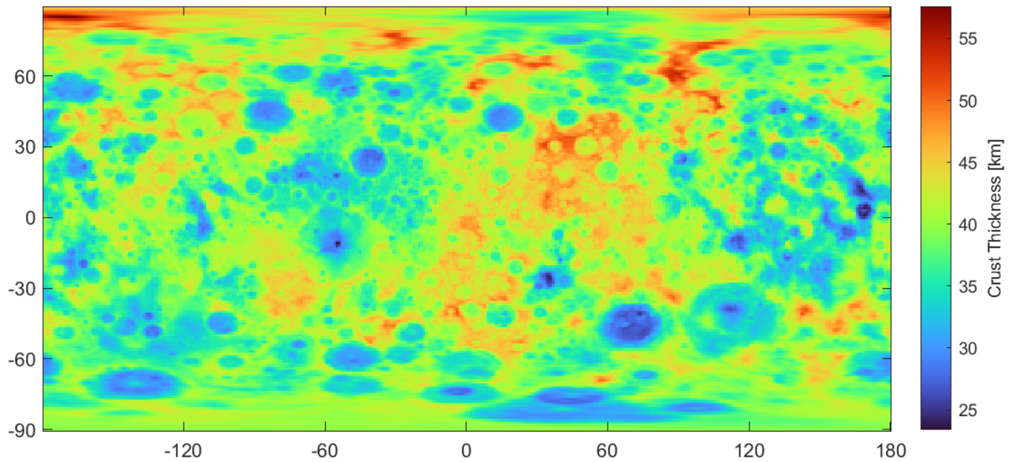

(a) Crust thickness of the selected Airy model.

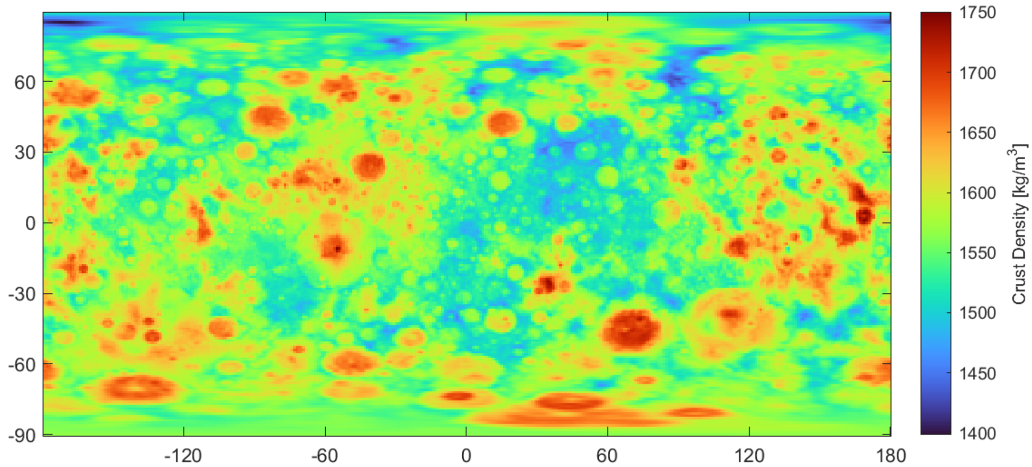

(b) Crust density of the selected Pratt model.

Figure 3.13: Crust models of the selected models.

The gravity residuals of the selected Airy and Pratt models are shown in Figure 3.14. It is visible that the residuals are practically the same, indicating that both models perform similarly in explaining the observed gravity signal. Although the range of the gravity residual (-70 to +80 mGal) is smaller than that of the original signal (-150 to +100 mGal), the positions of the extremes are different. Both models have a mean residual of approximately -4.45 mGal. Ceres' north pole has a much weaker gravity than is expected from its high topography, and similarly, there are a number of areas in the eastern hemisphere that exhibit a much stronger gravity than expected. Overall, except for a few places where the residual is very high, the gravity signal is much closer to 0 than in the original signal. The crust models therefore perform better than might be concluded from the range of the signal.

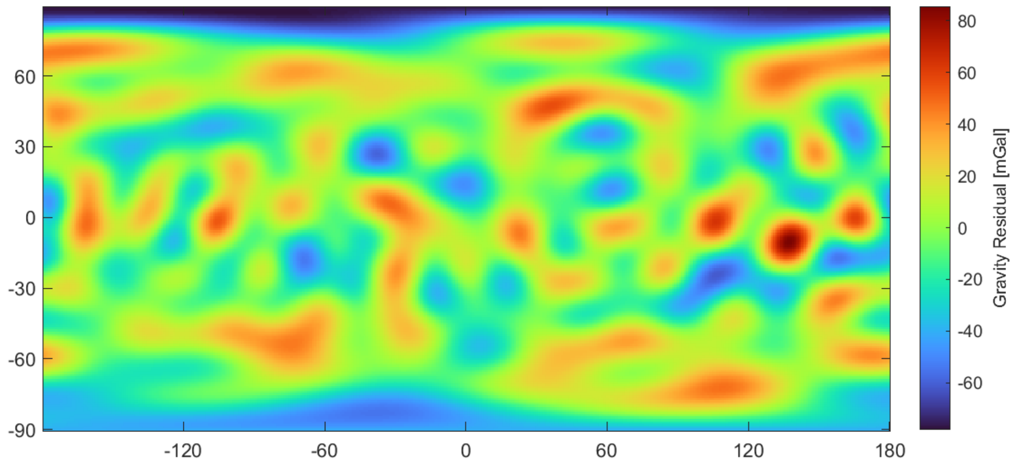

(a) Gravity residual of the selected Airy model.

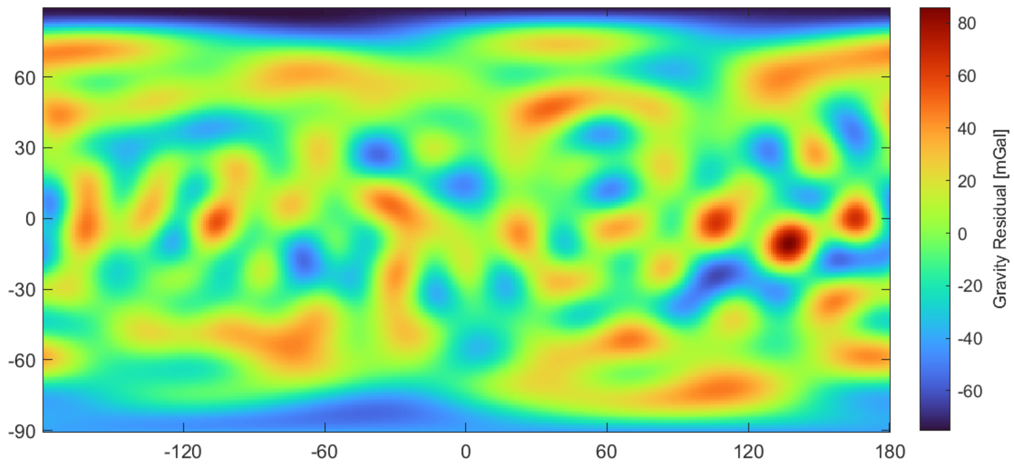

(b) Gravity residual of the selected Pratt model.

Figure 3.14: Gravity residuals of the crust model. Only spherical harmonic degrees 5-14 are included.

The density, gravity and pressure in Ceres' interior for the two models are shown in Figure 3.15. Here, it is observed that there is hardly any difference between the models in terms of the core pressure.

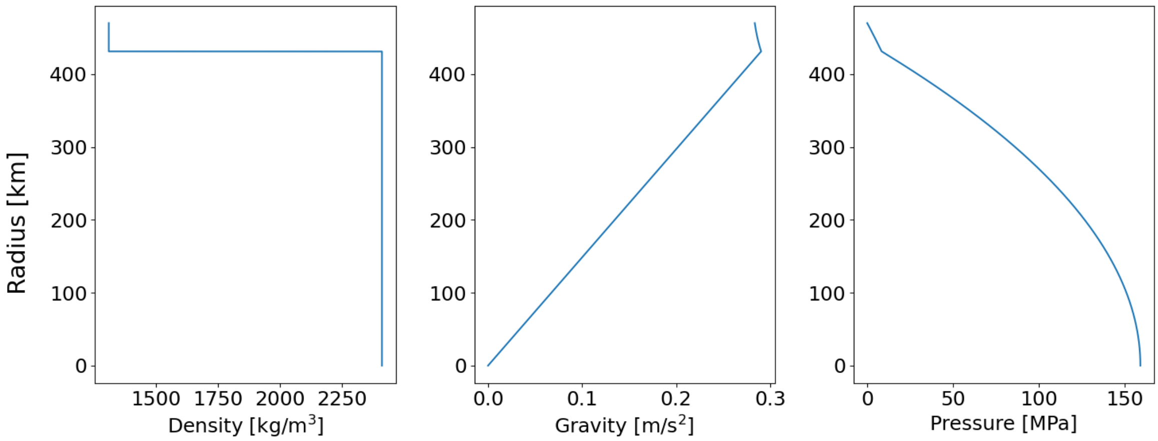

(a) Interior properties of the Airy model.

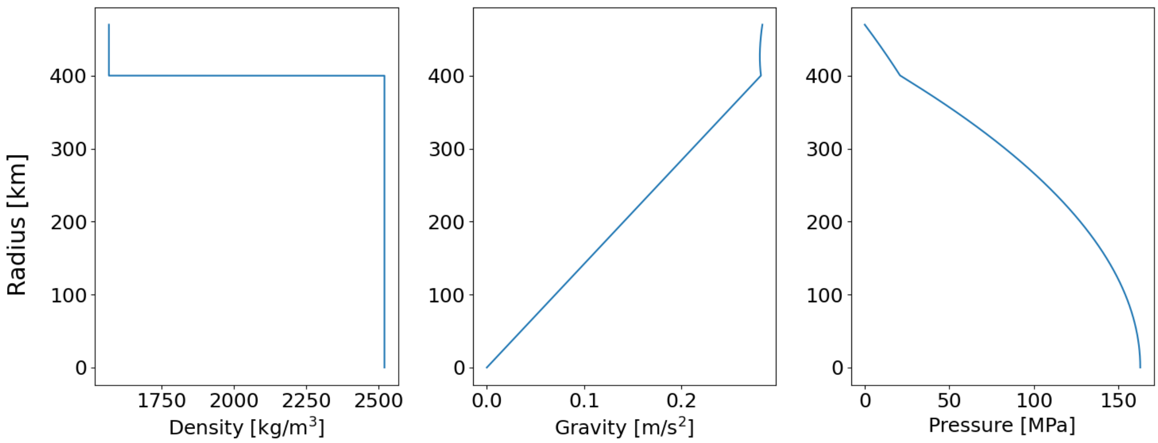

(b) Interior properties of the Pratt model.

Figure 3.15: 1D density, gravity and pressure in Ceres' interior as a function of radius for the two different models.

When comparing the values of the 1D structure associated with these crust models (summarized in Table 3.1), with those from literature, given in Table 1.1, it is found that in general the Airy model is more in line with the results of recent research. Furthermore, it is possible to interpret the composition of the layers based on their densities. The mantle densities are quite close to the density of serpentinite, 2600 kg/m^3. That the densities are a bit lower indicates that there are lighter materials in there, such as water (ice) or salts. The crust densities are significantly higher than that of water ice, indicating a high rock and/or salt content, as stated earlier.

Finally, the residual of the gravity field including all spherical harmonic degrees after taking into account the crust model is shown in Figure 3.16. It reveals a banded pattern of regions with stronger and weaker gravity, possibly indicative of a degree 2 convection cell. This residual field of the entire spectrum can be inverted back into changes in density in the isostasy models, assuming that the entire gravity field is due to the crust. This way, the lowest degrees of gravity field are included despite not being used to fit the isostasy models. The inverted density distributions are shown in Figure 3.17.

Table 3.1: Summary of the values of the 1D structure for the selected crust models.

Input Variable	Airy	Pratt
Crust Thickness km	39	70
Crust Density kg/m^3	1310	1570
Mantle Density kg/m^3	2410	2520

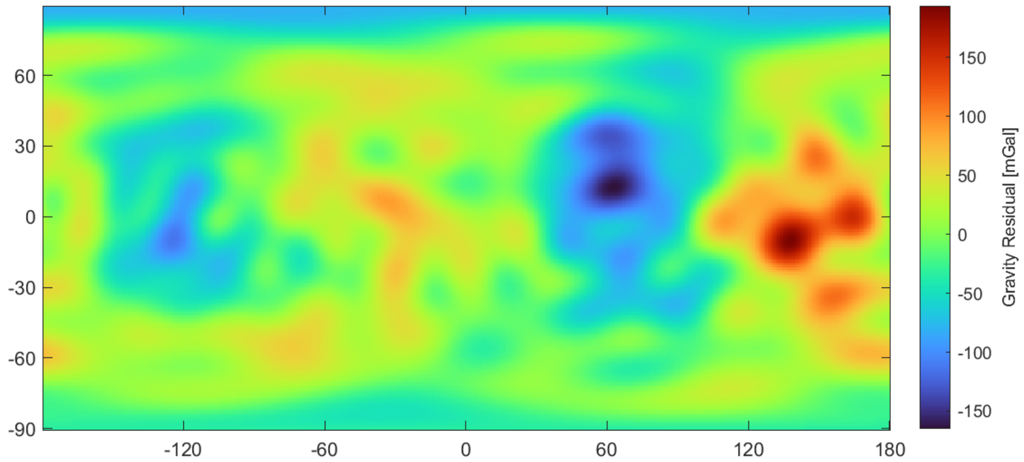

Figure 3.16: The residual of the gravity field of the Pratt model (which is approximately the same as that of the Airy model), including all spherical harmonic degrees.

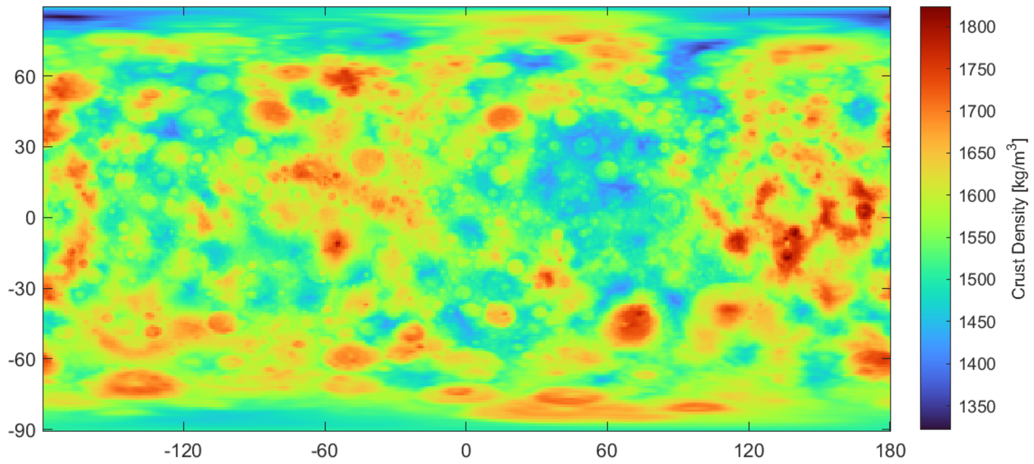

(a) Density distribution found by inverting the Pratt model.

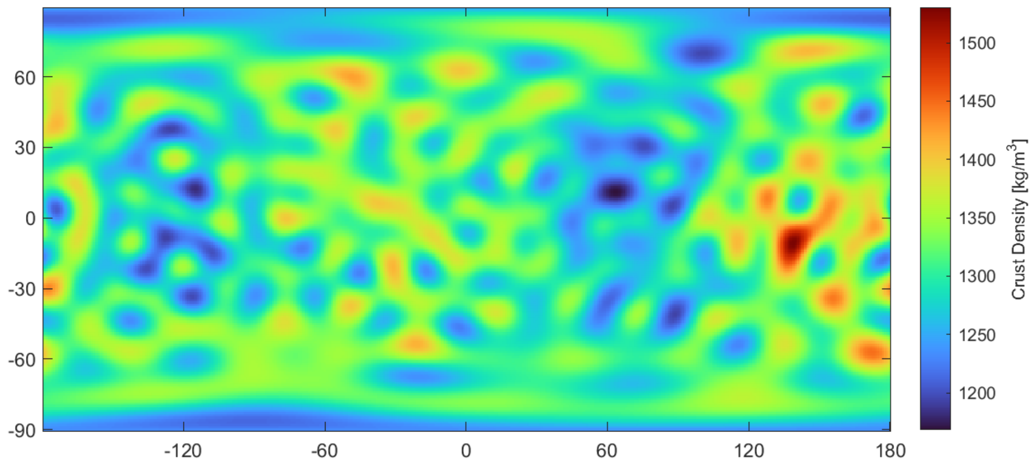

(b) Density distribution found by inverting the Airy model.

Figure 3.17: Density distributions obtained by inverted gravity residuals for density.

In Figure 3.17a, the banded pattern is now visible in the density distribution, because it is not solely dependent on the topography anymore. The densities of the Pratt crust model after inversion are between 1300 kg/m^3 and 1800 kg/m^3. The disparity in the density is smaller in Figure 3.17b, as most of the gravity field is explained by the crust thickness. Additionally, there appears to be quite a bit of noise in the otherwise familiar banded pattern, suggesting that this result is not particularly valid. The densities after inversion of the Airy model range from 1150 kg/m^3 to 1550 kg/m^3.

3.4. Thermal Profile

The thermal profile is a solution of the equation of conservation of energy. If a steady-state where there is no flow and only radiogenic heating is assumed this equation reduces to Equation 3.17. In this equation, κ is the thermal diffusivity and H is the volumetric radiogenic heating rate. The thermal diffusivity, in turn, is given by Equation 3.18, where k is the material's conductivity, ρ is its density, and C_p is its heat capacity, assumed to be constant across the material. The volumetric radiogenic heating rate H is considered a free variable.

$$-H = \nabla \cdot (\kappa \nabla T) \tag{3.17}$$

$$\kappa = \frac{k}{\rho C_p} \tag{3.18}$$

Taking only the radial component of Equation 3.17 in spherical coordinates results in Equation 3.19.

$$-H = \frac{1}{r^2}\frac{\partial}{\partial r}\left(\kappa r^2 \frac{\partial T}{\partial r}\right) \tag{3.19}$$

Rearranging the equation results in:

$$-Hr^2 = \frac{\partial}{\partial r}\left(\kappa r^2 \frac{\partial T}{\partial r}\right). \tag{3.20}$$

Integrating both sides of the equation yields:

$$-\frac{1}{3}Hr^2 + c_1 = \kappa r^2 \frac{\partial T}{\partial r}. \tag{3.21}$$

This equation can be rearranged to isolate $\frac{\partial T}{\partial r}$ and then integrated again to get:

$$T(r) = -\frac{Hr^2}{6\kappa} - \frac{c_1}{\kappa r} + c_2. \tag{3.22}$$

Equation 3.22 can be used to calculate the temperature of the Ceres' interior as long as the material properties remain the same, meaning that separate solutions are necessary for the crust and the mantle. Therefore, 4 boundary conditions are necessary to specify the values of the 4 integration constants $c_{1,m}$, $c_{2,m}$, $c_{1,c}$, and $c_{2,c}$, where the subscripts c and m signify the crust and mantle, respectively.

As no heat can be transferred out of the system at $r = 0$, from assuming that $\frac{\partial T}{\partial r} = 0$ there it can be readily deduced that $c_{1,m} = 0$.

Assuming continuity of the derivative of the temperature across the crust-mantle interface ($r = r_{bound}$) then leads to:

$$-\frac{H_m r_{bound}}{3\kappa_m} = -\frac{H_c r_{bound}}{3\kappa_c} + \frac{c_{1,c}}{\kappa_c r_{bound}^2}. \tag{3.23}$$

Rearranging this equation leads to Equation 3.24, which can be used to determine the value of $c_{1,c}$.

$$c_{1,c} = \frac{r_{bound}^3}{3}\left(H_c - \frac{\kappa_c}{\kappa_m}H_m\right) \tag{3.24}$$

The surface temperature $T_{surface}$ is found by using Equation 3.25 (Lissauer & de Pater, 2019), in which F_{sun} is the solar constant, $r_{aun_{AU}}$ is the distance from the sun to the body in question in astronomical units, A_b is the albedo, ϵ is the emissivity of the body and σ is the Stefan-Boltzmann constant.

$$T_{surface} = \left(\frac{F_{sun}}{r_{sun_{AU}}^2}\frac{(1 - A_b)}{4\epsilon\sigma}\right)^{1/4} \tag{3.25}$$

Imposing this boundary condition on the temperature profile leads to the following:

$$T_{surface} = -\frac{H_c R^2}{6\kappa_c} - \frac{c_{1,c}}{\kappa_c R} + c_{2,c}, \tag{3.26}$$

which can be rearranged into an expression for the $c_{2,c}$:

$$c_{2,c} = T_{surface} + \frac{H_c R^2}{6\kappa_c} + \frac{c_{1,c}}{\kappa_c R}. \tag{3.27}$$

The temperature at the mantle-crust boundary, T_{bound}, can then be found using the coefficients for the crust:

$$T_{bound} = -\frac{H_c r_{bound}^2}{6\kappa_c} - \frac{c_{1,c}}{\kappa_c r_{bound}} + c_{2,c}, \tag{3.28}$$

and used to constrain the temperature profile of the mantle:

$$T_{bound} = -\frac{H_m r_{bound}^2}{6\kappa_m} + c_{2,m}, \tag{3.29}$$

leading to:

$$c_{2,m} = T_{bound} + \frac{H_m r_{bound}^2}{6\kappa_m}. \tag{3.30}$$

The values for the variables used in the thermal profile are given in Table 3.2. The thermal properties of the mantle are chosen based on the assumption that it consists of serpentinite for such a large part that its properties are approximately the same as that of pure serpentinite. The fraction of serpentinite in the crust, f_s, is calculated using its density under the assumption that the crust is made up only of ice (subscript i) and serpentinite (subscript s), shown in Equation 3.31. This fraction is then used to calculate the thermal diffusivity of the crust using the rule of mixtures (Equation 3.32).

$$f_s = \frac{\rho_c - \rho_i}{\rho_s - \rho_i} \tag{3.31}$$

$$\kappa_c = f_s \kappa_s + (1 - f_s)\kappa_i \tag{3.32}$$

Table 3.2: Input values for the thermal profiles.

Variable	Symbol	Value
Albedo	A_b	0.09 (Li et al., 2006)
Heat capacity of the mantle	$C_{p,m}$	1000 J/K (Osako et al., 2010)
Heat capacity of ice	$C_{p,i}$	1389 J/K (“Ice - Thermal Properties”, n.d.)
Solar constant	F_{sun}	$1.37 \cdot 10^3$ W/m^2 (Lissauer & de Pater, 2019)
Thermal conductivity of the mantle	k_m	2.7 W/mK (Osako et al., 2010)
Thermal conductivity of ice	k_i	3.48 W/mK (“Ice - Thermal Properties”, n.d.)
Distance from the sun	$r_{sun_{AU}}$	2.77 AU (Lissauer & de Pater, 2019)
Thermal emissivity	ϵ	1 - A_b
Density of ice	ρ_i	917 kg/m^3
Density of serpentinite	ρ_s	2600 kg/m^3
Stefan-Boltzmann constant	σ	$5.67 \cdot 10^{-8}$ W/m^{2}K (Lissauer & de Pater, 2019)

Finally, it is assumed that all of the radioactive elements are contained within the serpentinite, so that the heating in the crust is proportional to the serpentinite fraction:

$$H_c = f_s H_s = f_s H_m. \tag{3.33}$$

Therefore, the only free variable left is H_m, which can be varied to analyse the plausibility and likeliness of a liquid (muddy) ocean on Ceres.

4

Verification and Validation

In order to gain insight into the performance of isostasy-based crust models, different models of the Earth's crust thickness are compared against the measured thickness. These measured thicknesses are obtained by adding the Earth's topography (Hirt & Rexer, 2015) to its seismic moho depth (Szwillus et al., 2019).

As Earth's crust is more suitable for Airy compensation, Pratt compensation is not considered. To compare the relative performance of different Airy-based approaches, models of the entire crust of the Earth are made using the input values given in Table 4.1. The young's modulus E and Poisson ratio ν of the lithosphere material are determined from the bulk and shear moduli by solving the system of equations given by Equation 4.1 and Equation 4.2.

Table 4.1: Input values for the models comparing the different modelling approaches.

Variable	Symbol	Value
Reference Depth	-	24 km
Mantle Density	ρ_m	3320 kg/m^3 ("Olivine Mineral Data", n.d.)
Crust Density	ρ_c	2835 kg/m^3 (Christensen & Mooney, 1995)
Elastic Thickness	T_e	34 km (Watts & Moore, 2017)
Bulk Modulus	K	128.8 GPa (Z. Mao et al., 2015)
Shear Modulus	S	81.6 GPa (Z. Mao et al., 2015)

$$K = \frac{E}{3(1-2\nu)} \tag{4.1}$$

$$S = \frac{E}{2(1+\nu)} \tag{4.2}$$

To find out how strongly the input variables affected the model, each of them was varied around the starting value to find how the root-mean-square-error was affected. The results showed that the bulk and shear modulus have a much weaker effect than the other variables, in fact being almost negligible. Therefore, it was not included in further investigations on optimal input values.

The root-mean-square-error of the different modelling approaches, using the input values given in Table 4.1, are given in Table 4.2. The error of the best performing model, the thin shell flexure model based on the equal pressures airy model, is shown in Figure 4.1.

Table 4.2: root-mean-square-error of the different modelling approaching using the input values in Table 4.1.

Model	RMSE km
Equal Masses	6.6833
Equal Pressures	6.6683
Infinite Plate (Equal Masses)	6.4946
Infinite Plate (Equal Pressures)	6.4826
Thin Shell (Equal Masses)	6.3682
Thin Shell (Equal Pressures)	6.359

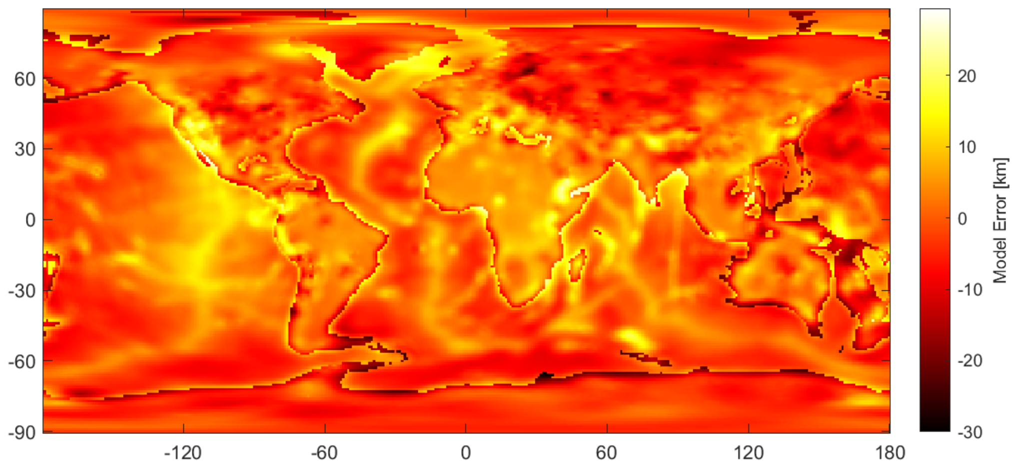

(a) Error in kilometers with respect to the measured crust thickness.

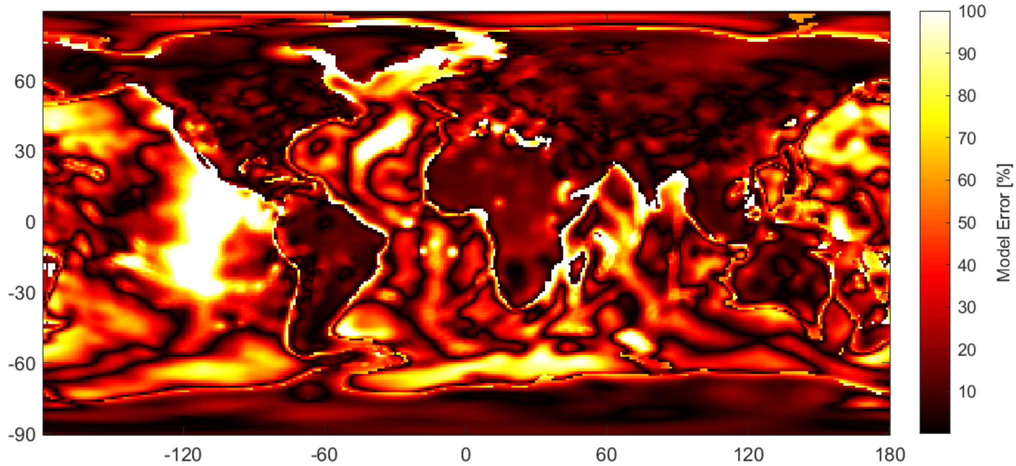

(b) Error in percentages of the measured crust thickness (capped at 100%).

Figure 4.1: Error of the thin shell flexure model based on the equal pressures airy model.

From Table 4.2, it can be clearly seen that the more complicated models perform better than the simpler ones, which include more assumptions. This is to be expected, but the increase in accuracy is rather small because the simplifying assumptions for the simpler models are quite valid for the Earth. For smaller bodies, where the crust thickness is a more significant fraction of the radius, the error introduced by these assumptions will be more significant. Therefore, the more complex models will be more appropriate for modelling Ceres' crust. Furthermore, when examining the difference in root-mean-square-error between the flexure models, it can be noted that the effect of changing between infinite plate and thin shell modelling is greater than changing between equal masses and equal pressures.

An interesting feature to be noted from Figure 4.1a is that the model greatly overestimates that thickness of the crust at the mid-ocean ridges. That the crust would be thinner than expected from the model at these locations can be attributed to the non-isostatic nature of the tectonic processes by which the plate material forms at the mid-ocean ridges. Figure 4.1b shows that the error as a percentage of the crust thickness is reasonably low and constant for continental crust, and more variable and at some places very high for oceanic crust. This indicates that isostasy models are more appropriate for modelling continental crust than oceanic crust. Due to the absence of plate tectonics on Ceres, its crust is expected to behave more like continental crust than oceanic crust, adding credence to the suitability of isostasy models for modelling Ceres' crust.

Because of the large observed disparity of the performance of the model between the continental and oceanic crust, the difference in performance between models made for different continental crust types is investigated. To do this, a thin shell flexure model based on an equal pressures airy compensated crust is made for crust of four thermo-tectonic ages. These thermo-tectonic ages, in order from oldest to youngest, are the Archean, the Proterozoic, the Paleozoic, and the Meso- and Cenozoic. A map of where crust of each of these ages can be found is taken from Goutorbe et al. (2011) (shown in Figure 4.2), and a model is optimized for each of these data sets. The optimization process is successive in order to minimize computational effort, and it prioritizes the variables with the largest effect. First, the reference depth that leads to the lowest root-mean-square-error is selected, after which a grid search is performed to find the optimal combination of mantle and crust densities. Finally, the elastic thickness that minimizes the root-mean-square-error is taken. The starting values, search range and search resolution are summarized in Table 4.3. The starting values of the variables are based on the optimal values found for a single model of the entire continental crust, found by the same optimization procedure. The resulting models are used to characterize the error associated with each of the crust ages.

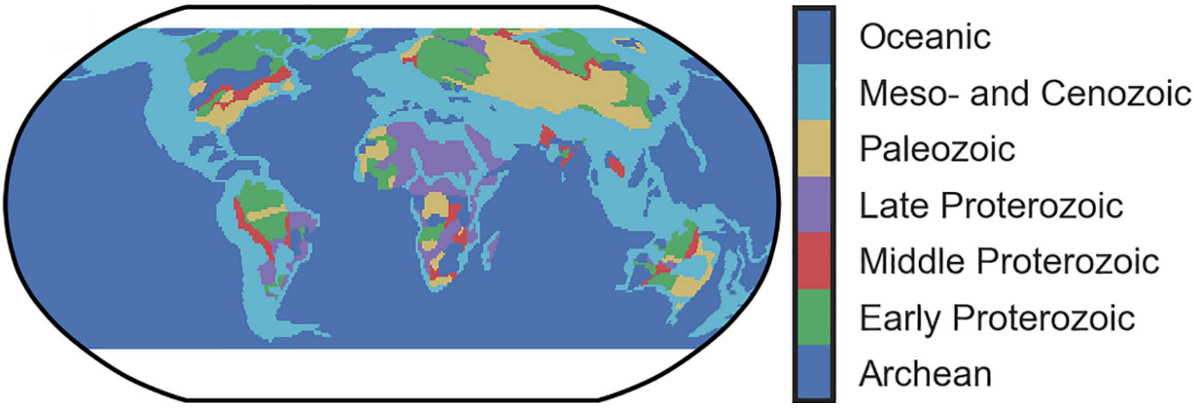

Figure 4.2: Thermo-tectonic ages of the Earth's crust (Szwillus et al., 2019).

Table 4.3: Parameters for the optimization of the models for different crust types.

Variable	Starting Value	Range	Resolution
Reference Depth	32 km	25-40 km	1 km
Mantle Density	2700 kg/m^3	1200-5200 kg/m^3	100 kg/m^3
Crust Density	1900 kg/m^3	700-3400 kg/m^3	100 kg/m^3
Elastic Thickness	80 km	20-120 km	1 km

For the composite model that combines seperate models for different thermo-tectonic ages, the root-mean-square-error and average percentage error for each crust type and the total root-mean-square-error are given in Table 4.4. The error of the full model is shown in Figure 4.3.

Table 4.4: root-mean-square-error and average percentage error of the different thermo-tectonic ages of the crust.

Crust Age	RMSE km	Average Percentage Error
Meso- and Cenozoic	6.7294	18.1%
Paleozoic	4.3471	8.2%
Proterozoic	4.7151	9.2%
Archean	3.7582	6.9%
Total	5.7612	13.5%

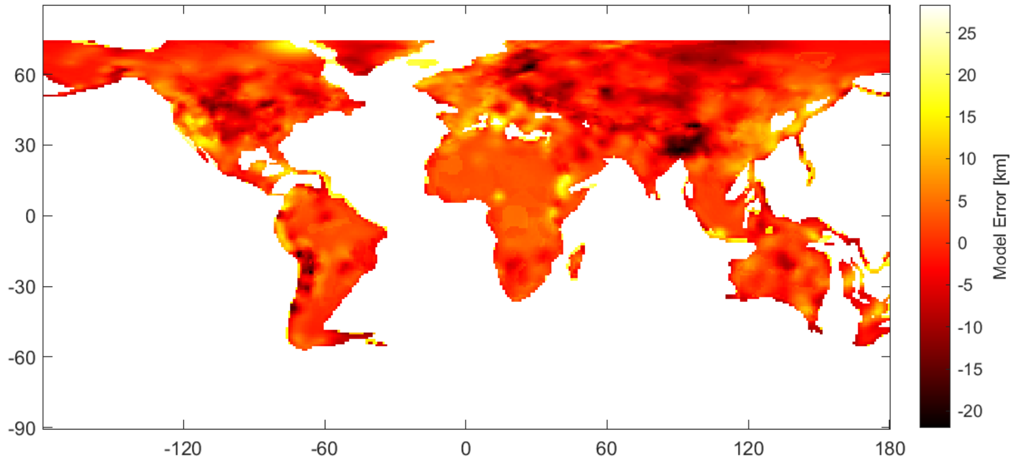

(a) Error in kilometers with respect to the measured crust thickness.

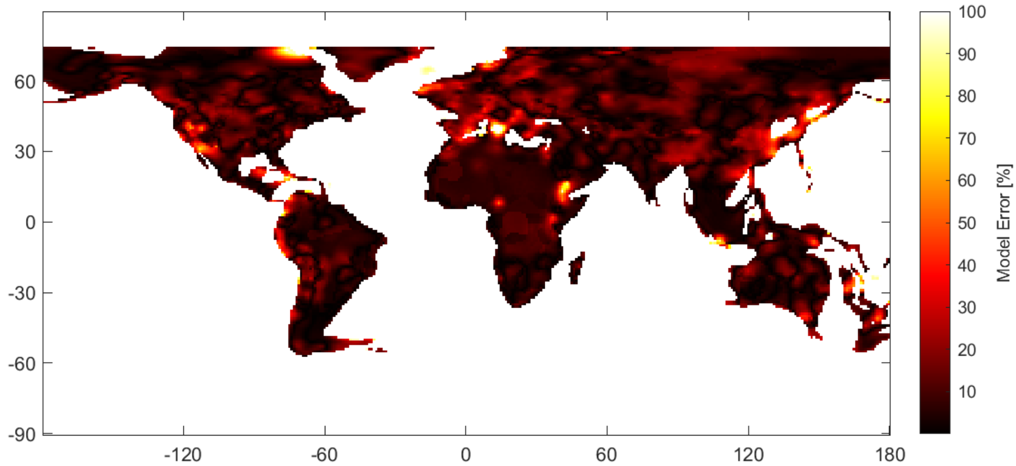

(b) Error in percentages of the measured crust thickness.

Figure 4.3: Error of the composite crust model.

In Table 4.4, a general trend can be observed where isostasy models perform better for older crust. This is advantageous, because the absence of plate tectonics make Ceres' crust likely to behave more like Earth's older crust. Furthermore, the complete composite model makes an average error of 13.5%, but when viewing Figure 4.3b, it is clear that this number is significantly affected by a number of outliers, and that for the majority of the crust, the error is below 10%. Nevertheless, the average percentage error can be used a useful metric to characterize the expected error of an isostasy model of Ceres' crust.

Furthermore, the validity of the developed models can be investigated by comparison of its results to those from literature. In Figure 4.4, the crust thickness of the Airy model in this work is shown alongside the crust thickness of an isostatic model from Ermakov et al. (2017). From the range of the crust thicknesses, it is already visible that the found thicknesses are very comparable. Furthermore, upon further inspection, it is clear that the features of the maps are very similar, differing only slightly in the extremes in some areas, such as the poles. The large degree of similarity between the model in this work and that of the previous work implies that the model in this work is valid.

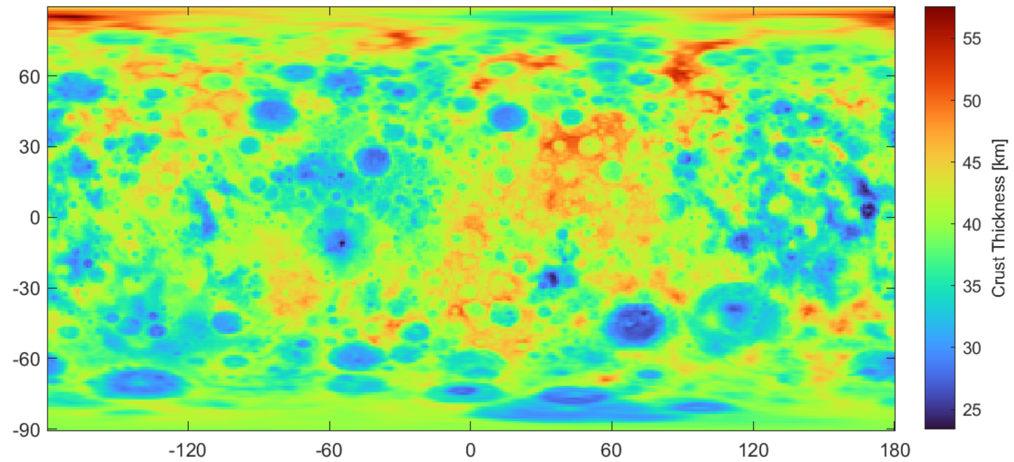

(a) Crust thickness of the Airy model in this work.

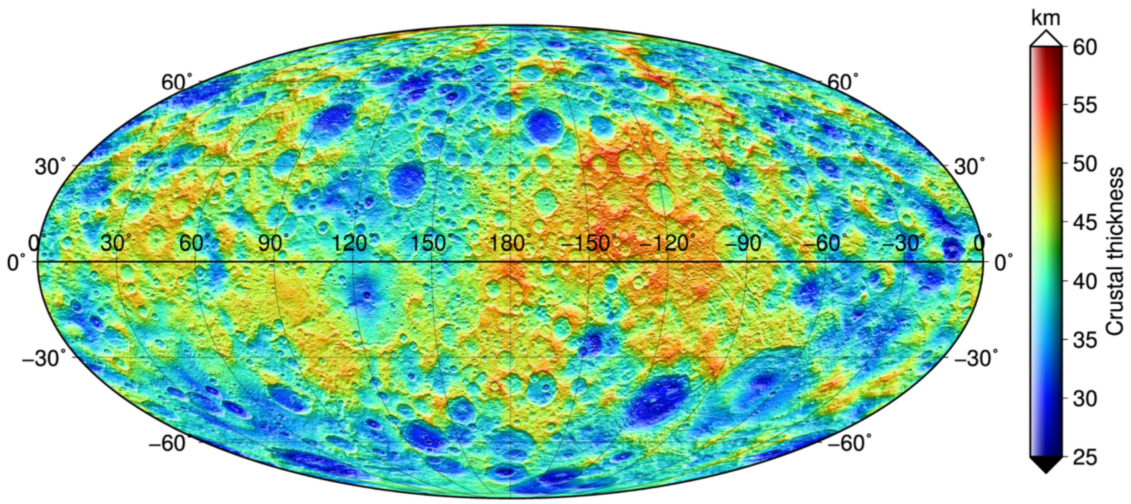

(b) Crust thickness from Ermakov et al. (2017).

Figure 4.4: Crust thicknesses from this work and from literature for the purpose of comparison.

5 Results

To reiterate, the Pratt model after inversion has crust densities between 1300 kg/m^3 and 1800 kg/m^3, while the Airy model has crust thicknesses between 24 km and 57 km and crust densities from 1150 kg/m^3 to 1550 kg/m^3.

To assess the correlation between the crustal properties and observations of cryovolcanism, a dataset of locations of bright spots on Ceres' surface (Stein et al., 2019) is used to find the crustal properties that correspond to the locations of cryovolcanic observation. This dataset is the result of a global bright spot mapping study between the latitudes of -60° and 60°. When these properties are found, a histogram is made to visualize the distribution of the data. The maps of the bright spots over crustal properties are shown in Figure 5.1. Judging from these maps, there does not seem to be a particular correlation with these crust properties.

The histograms showing the distribution of these observations are shown in Figure 5.2. In these figures, the blue bars represent the amount of bright spots associated with that particular value of the crustal property. The red line indicates how the distribution would look if it followed a normal distribution, consistent with a random error around a mean value. The green line indicates how the distribution of the entire crust, not just those points associated with cryovolcanism, would look like if it were a normal distribution.

All of these histograms show that the distribution of the observations is fairly in accordance with a normal distribution and that the mean values of the observations do not differ significantly from those of the entire crust at large. This indicates that there is not a strong correlation between the crustal properties and the bright spots.

Interestingly, the crust density in the Airy model shows extremely little difference between the full crust and only cryovolcanic observations compared to the other crust properties. The densities in this model are obtained through inverting the gravity signal and are therefore only dependent on gravity and not topography, suggesting that the gravity data is not very useful for modelling the interior.

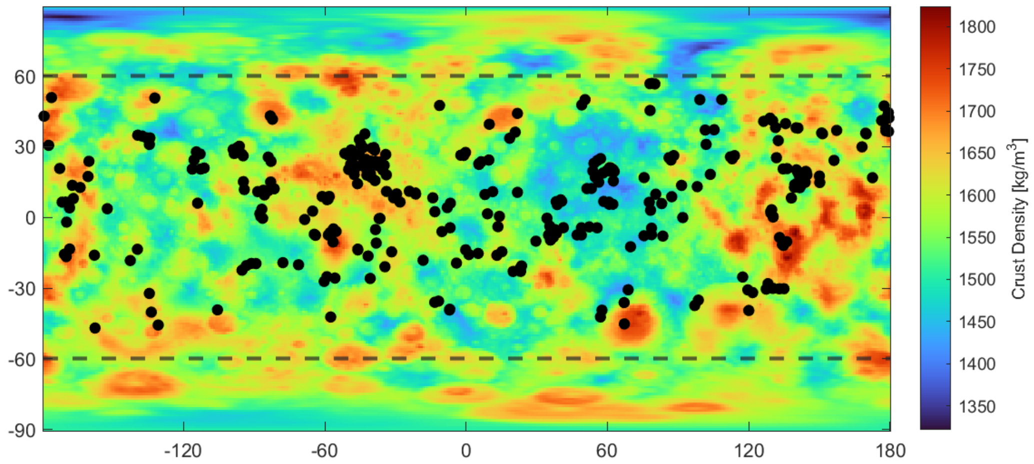

(a) Cryovolcanic locations overlaid over map of crust densities obtained by inverting the Pratt model.

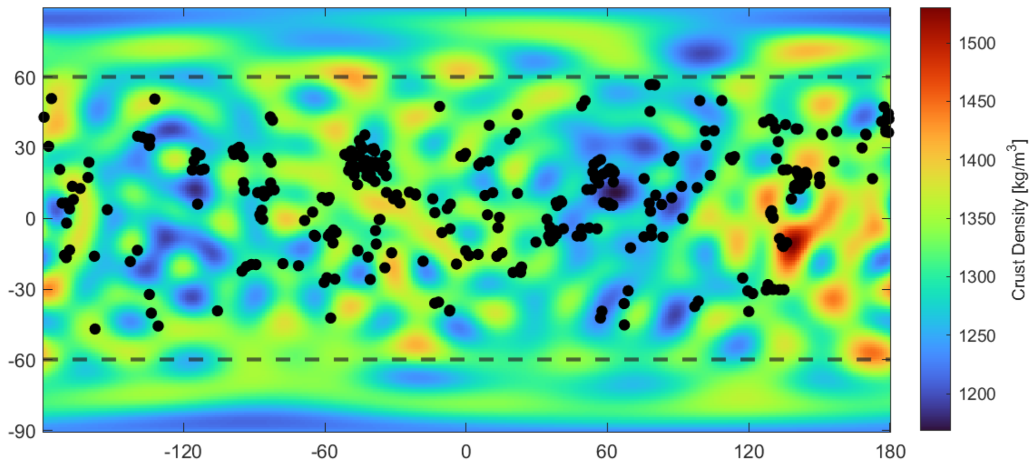

(b) Cryovolcanic locations overlaid over map of crust densities obtained by inverting the Airy model.

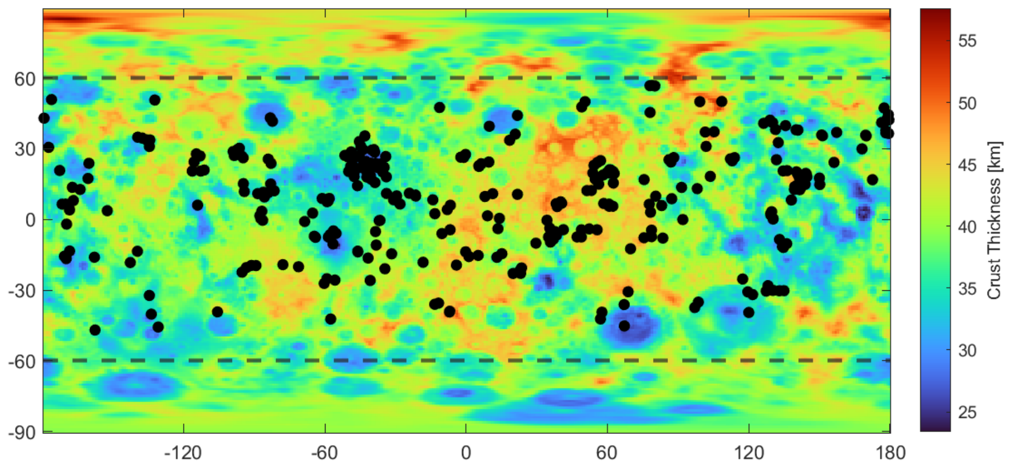

(c) Cryovolcanic locations overlaid over map of crust thicknesses from the Airy model.

Figure 5.1: Cryovolcanic observation maps.

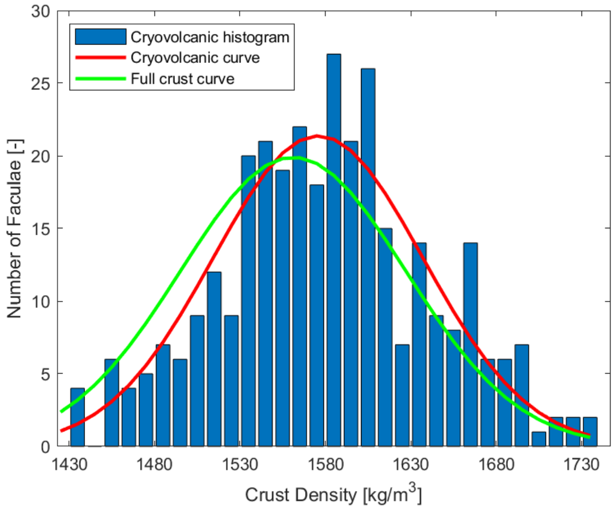

(a) Histogram of crust density from inverting Pratt model.

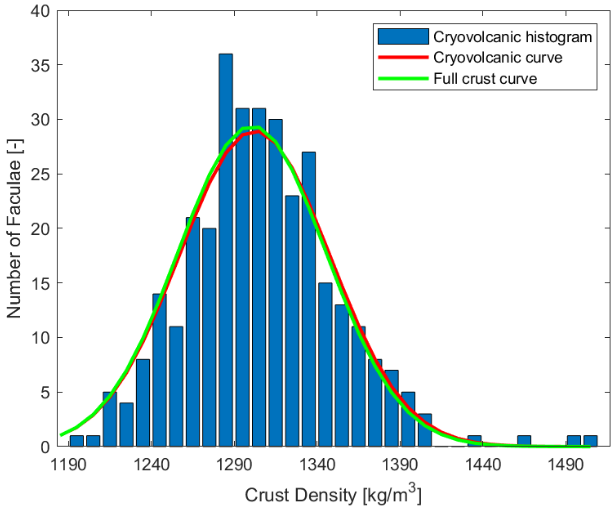

(b) Histogram of crust density from inverting Airy model.

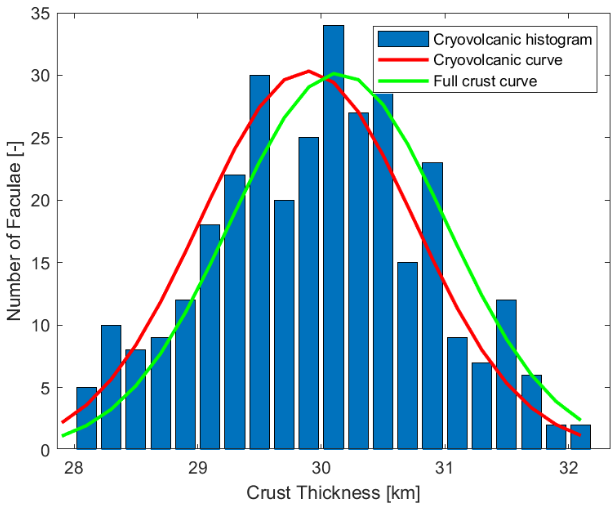

(c) Histogram of crust thickness from Airy model.

Figure 5.2: Histograms of crustal properties corresponding to observations of cryovolcanism. The red curves are the gaussian curves based on the datasets mean and standard deviation, indicating the expectation of the distribution if there was random error about the mean value. The green curves are the gaussian curves based on the entire dataset of the crust, signifying the distribution if there is no correlation between the crustal property and the cryovolcanism.

Next, the possibility of liquid water in the crust must be investigated. Figure 5.3 shows the effect of the volumetric heat generation rate H on the 1D temperature profile of the planet. The values of H are chosen to demonstrate the amount of internal heating necessary for the possibility of liquid water to exist in the crust without the necessity of impact heating for different levels of dissolved salt. The melting temperatures of ice were calculated using a dataset on the melting temperature at different pressures [1], and the simple relation in Equation 5.1 [2], in which ΔT_f is the amount by which the melting temperature decreases, c_f is the melting temperature depression constant of the solvent (1.86 K/mol for water), μ is the molality of the solution, and i is the number of particles formed when the solute dissolves. The molality is calculated using Equation 5.2, in which m_{solute} is the mass of solute in the solution, M_{molar} is the molar mass of the solute (58.443 g/mol for NaCl), and $\rho_{solvent}$ is the density of the solvent.

$$\Delta T_f = c_f \mu i \tag{5.1}$$

$$\mu = \frac{m_{solute}}{M_{molar}\rho_{solvent}} \tag{5.2}$$

The different values of the salinity in Figure 5.3 correspond to 0%, 50% and 100% of the solubility of NaCl.

In Figure 5.3a, showing the thermal profile for the Pratt-based density profile, it is visible that for a heating rate of $1.3 \cdot 10^{-14}$ W/m^3 or higher, the temperature is certainly high enough for liquid water to exist in the crust.

For the Airy-based model a higher value for the heating rate is necessary to allow for liquid water in the crust, shown in Figure 5.3b. This is largely due to the smaller crust thickness, meaning that a higher temperature is necessary further from the planetary center. Additionally, as the crust material is lighter, the crust is under less pressure, raising the melting temperature of the ice. The lighter material also implies a lower fraction of serpentinite and therefore less radiogenic heating in the crust.

The value of the volumetric heating rate can be compared to the expected volumetric heating rate in other terrestrial bodies, such as in the models for Mars made by Breuer et al. (2022), where it is found to be of the order of 10^{-12} W/m^3. The heating rate necessary for liquid water in the crust, then, is significantly smaller than a typical value.

[1] https://www.engineeringtoolbox.com/water-melting-temperature-point-pressure-d_2005.html, retrieved August 29th 2024

[2] https://chem.libretexts.org/Bookshelves/Introductory_Chemistry/Introductory_Chemistry/13%3A_Solutions/13.09%3A_Freezing_Point_Depression_and_Boiling_Point_Elevation, retrieved August 29th 2024

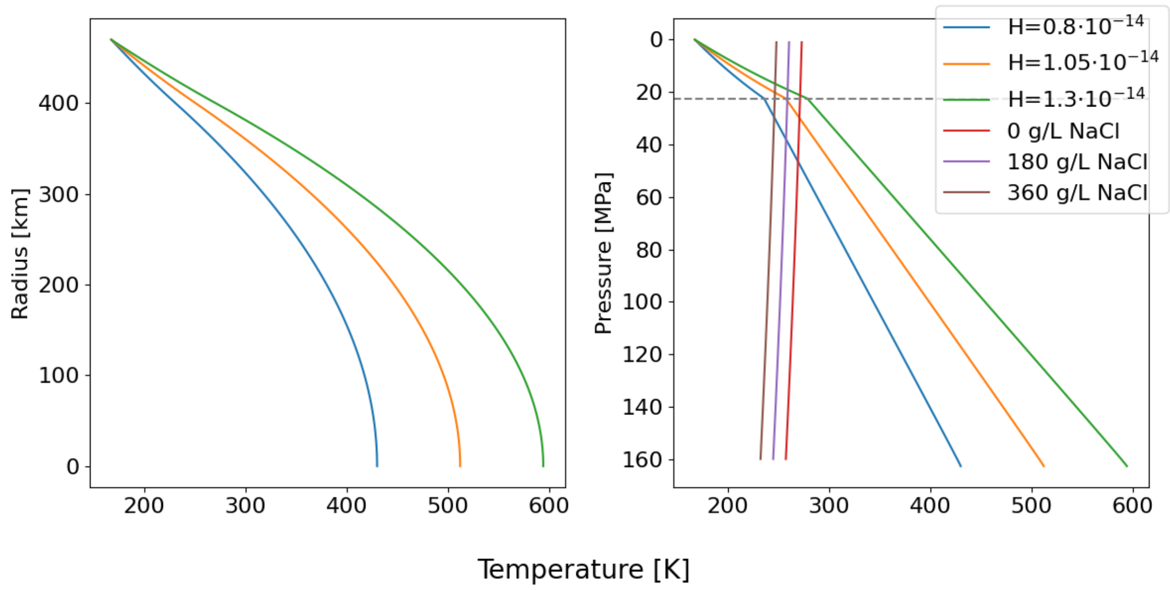

(a) Temperature profile and PT diagram for the density profile corresponding to the Pratt model.

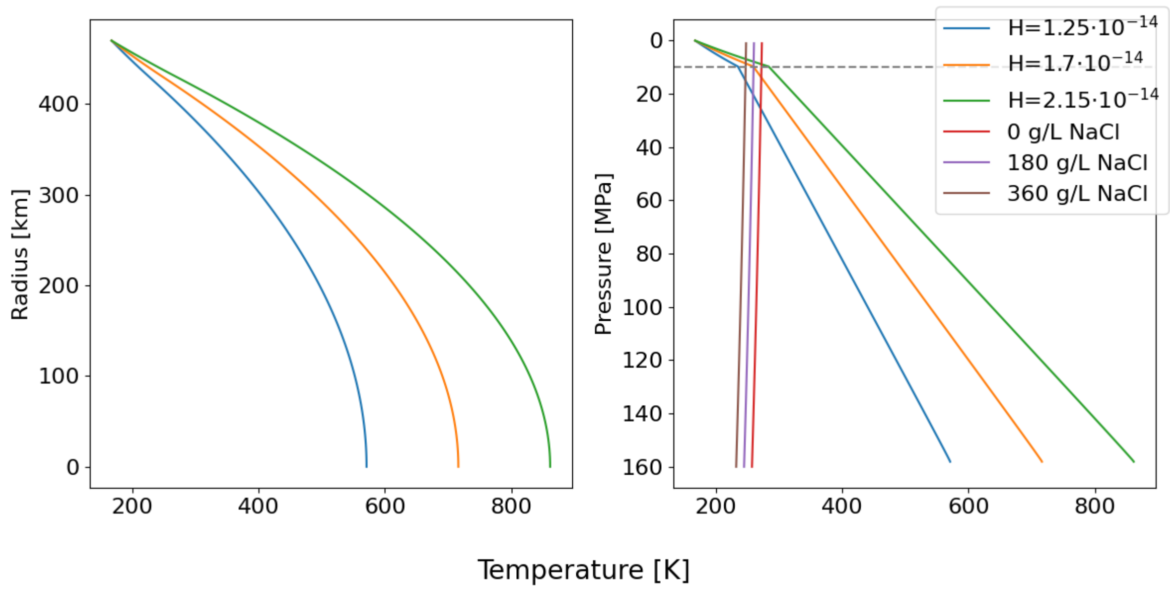

(b) Temperature profile and PT diagram for the density profile corresponding to the Airy model.

Figure 5.3: Temperature profiles and PT diagrams for different values of the serpentinite volumetric heat generation rate H in W/m^3. The PT diagrams also show the melting temperature for ice with different amounts of dissolved salt. The dashed line represents the mantle-crust boundary.

The temperature profiles found are reasonably close to those found in literature in terms of the surface and core temperatures, as seen for example in Figure 1.6. This confirms the validity of the profile to some extent.

6 Discussion

The weak correlation between bright spots and crustal properties implies that the brines necessarily present for the formation of the bright spots are not heterogeneously distributed. Therefore, this result contradicts the hypothesis that the bright spots are formed from sub-surface brine reservoirs that are hit by impacts. Rather, the brines would likely be more homogeneously distributed, such as in a sub-surface ocean or frozen into the ice.

From the thermal profiles, it is found that the temperature at the base of the crust is certainly high enough for the existence of liquid brine if the volumetric heating rate is higher than $2 \cdot 10^{-14}$ W/m^3. This value can be compared to the expected volumetric heating rate in other terrestrial bodies, such as in the models for Mars made by Breuer et al. (2022), where it is found to be of the order of 10^{-12} W/m^3. Therefore, if Ceres' interior is similar to that of the terrestrial planets, it is expected that the temperature inside the planet would be high enough that liquid brine would be present in Ceres' crust even without the need for impact heating.

Combining these two findings, the interpretation of the results of this work is that Ceres likely has a sub-surface ocean at the base of its crust. Due to the non-trivial rock content of its crust, this would be a very muddy ocean, with many suspended rock particles. The expected formation mechanism following from this information is shown diagrammatically in Figure 6.1. Here, impacts cause cracks in the crust, which allow for the already liquid brine to rise to the surface. The brine could be driven to rise to the surface due to some form of capillary action caused by the evaporation of impact-heated ice at the top of the crust or through pressurization of the ocean through successive refreezing of the ice at the bottom of the crust due to the interaction with the dissolved salts.

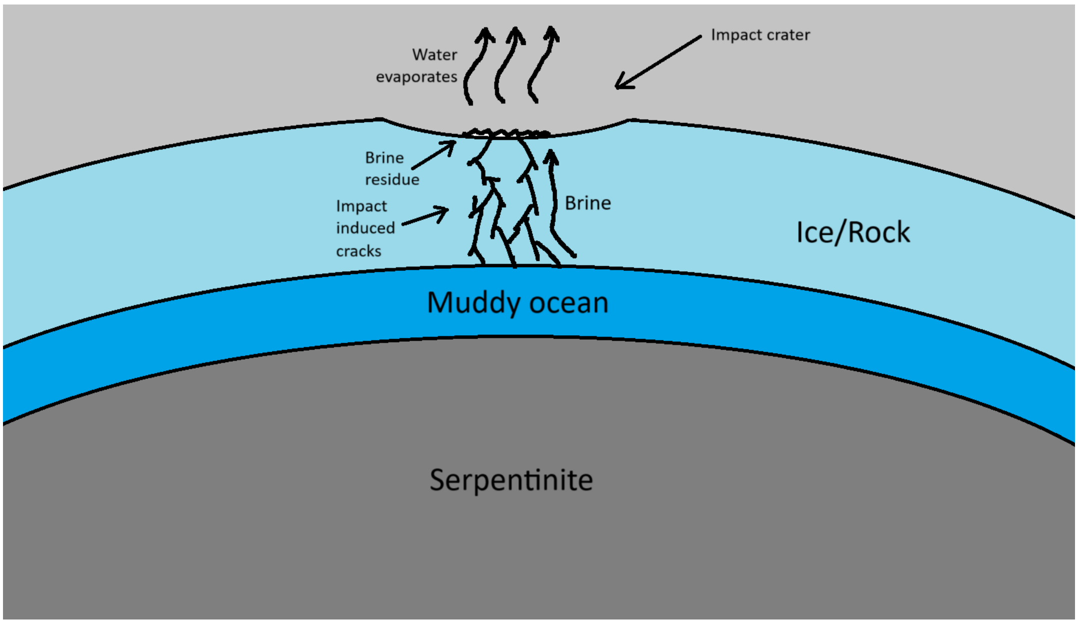

Figure 6.1: Diagram of the formation mechanism of the bright spots on Ceres' surface.

In this model, the entire inner layer is made of serpentinite, a hydrated silicate. This is due to the parsimony of a 2-layer model. However, it is very possible, and indeed maybe even likely, that there exists an even deeper layer of unhydrated silicate, such as olivine. The existence of a metal core, though less likely, is similarly possible, as the mass and moment of inertia requirements can be satisfied with any number of layers.

The thermal profile developed in this work assumes that there is no flow in the interior and that all heat transfer is conductive. Clearly, the existence of a muddy ocean in between the mantle and crust contradicts this assumption. Furthermore, it is possible that Ceres has a lower internal heating rate than other terrestrial bodies. This could be consistent with hypotheses that Ceres formed further out in the solar system and the fact that it has an uncharacteristically high amount of water for a terrestrial planet. Finally, this work assumes that a steady-state has been reached for the temperature in the interior, while there exists the possibility that the interior has not yet reached this steady state. This would lead to a higher temperature profile and more possibility for convection.

A similar assumption is present in the crust models, because they assume that every part of the crust is in isostatic equilibrium. Some parts of the crust, such as impact craters, could be young enough that isostatic equilibrium has not yet formed underneath. This might cause a bias in the crust properties associated with bright spots. Furthermore, the conclusion that brine is not heterogeneously distributed in Ceres' crust does not offer an explanation for why floor bright spots are formed inconsistently in impact craters.

The final model suggested by this work is very similar to the one proposed by Castillo-Rogez et al. (2019). This model also includes a mud layer between the crust and mantle and includes a similar final temperature profile, as shown in Figure 1.6. It differs, however, in where the boundary between the crust and mantle would be. In this work, it would be close to the depths of 70 km or 39 km, wheres in that of Castillo-Rogez et al. (2019) the mud layer is between 50 km and 90 km. Compared to the thermal models of Neumann et al. (2020), the final temperature profiles in this work are higher by 100 K to 200 K, and the formation mechanism for the bright spots are not consistent. In that study, the bright spots are hypothesized to be formed by heterogeneously distributed upwellings of brine, but this is contradicted by the low correlation between cyovolcanism and crustal properties found in this work.

A mud layer is consistent with findings by Ruesch et al. (2019), which indicate that cryovolcanism in Ahuna Mons and bright spots require a material that is essentially a convective slurry, with a significant amount of non-soluble solid particles. A mud layer would satisfy the requirements found in that work. Of course, the formation mechanism proposed here is not consistent with either of the ones proposed by Stein et al. (2019), because there are no subsurface brine reservoirs and impact heating is not necessary to melt the cryovolcanic material. However, the hypotheses agree on the idea that impacts form cracks through which cryovolcanic material can rise to the surface of the planet.

The results of this work imply that future research may be more relevant if they include a mud layer in their models and investigate the process by which the muddy ocean material rises to the surface, as well as why floor bright spots form inconsistently.

7 Conclusions

The goal of this work was to investigate the formation mechanism of the bright spots on Ceres' surface. In order to do so, interior models were developed and analyzed. Specifically, the following questions were answered:

1. What is the formation mechanism of the bright spots on Ceres?
   (a) To what degree is Ceres differentiated?
   (b) How accurate are isostasy-based crust models?
   (c) What are Ceres' crustal properties?
   (d) How correlated are the locations of bright spots and the crustal properties?
   (e) Under which conditions is no external energy source necessary for liquid brine to exist in Ceres' crust?

The answers to these questions are summarized here.

Ceres is most likely partially differentiated, with a silicate inner layer and an outer layer made of water ice mixed with silicates and dissolved salts and/or clathrates. These layers are also likely seperated by a muddy ocean layer, where the temperature is high enough to support liquid brines without external heat sources. This muddy ocean layer would have a significant amount of non-soluble solid particles suspended in it and would be similar to a slurry.

Isostasy-based crust models have been shown in this work to be able to predict crustal properties of Earth with an average error of 13.5%, as shown in Figure 4.3b. Their performance is observed to be related to the age of the crust, with the general trend being that it performs better for older types of crust. This is advantageous for modelling Ceres' crust, as Ceres lacks the tectonics that would make parts of the Earth's crust younger.

Ceres' crust densities vary between 1300 kg/m^3 and 1800 kg/m^3, with a mean value of 1560 kg/m^3, when using a Pratt model and inverting the gravity anomaly for density. This is shown in Figure 3.17a. When using an Airy model, shown in Figure 3.13a, the crustal thickness varies between 24 km and 57 km, with a mean value of 30 km.

No significant correlation is found between any of the crustal properties and the locations of bright spots on Ceres' surface. The distributions are very similar to normal distributions, and the means are very close to the means of the crust as a whole. This is shown in Figure 5.2.

Liquid brine can exist in Ceres' crust without external energy source when the internal heating rate is more than $2 \cdot 10^{-14}$ W/m^3, which is a low value for a terrestrial planet.

Taking all these results into account, the proposed formation mechanism of the bright spots (summarized in Figure 1.7) is that impacts forms cracks in the crust from the surface to a muddy sub-surface ocean, allowing the brine from this ocean to rise to the surface.

As the thermal modelling in this work does not take into account the effects of the muddy ocean hypothesized to exist based on the results of this work, this would be primarily recommended for future work to investigate. Furthermore, as it is not clear what drives brines to the surface of the planet from the muddy ocean, research into what could drive this phenomenon will be invaluable.

References

Ashby, M. F., Shercliff, H., & Cebon, D. (2014). *Materials : Engineering, science, processing and design* (Third edition, North American edition) [Section: xvi, 94, 27 pages, 95-596 pages, 71 pages, 597-637 pages, 19, 36 pages : illustrations ; 26 cm]. Elsevier Butterworth-Heinemann.

Bland, M. T., Raymond, C. A., Schenk, P. M., Fu, R. R., Kneissl, T., Pasckert, J. H., Hiesinger, H., Preusker, F., Park, R. S., Marchi, S., King, S. D., Castillo-Rogez, J. C., & Russell, C. T. (2016). Composition and structure of the shallow subsurface of ceres revealed by crater morphology. *Nature Geoscience*, *9*(7), 538–542. https://doi.org/10.1038/ngeo2743

Breuer, D., Spohn, T., Van Hoolst, T., van Westrenen, W., Stanley, S., & Rambaux, N. (2022). Interiors of earth-like planets and satellites of the solar system [ISBN: 0169-3298 Publisher: Springer]. *Surveys in Geophysics*, *43*(1), 177–226.

Castillo-Rogez, Hesse, M., Formisano, M., Sizemore, H., Bland, M., Ermakov, A., & Fu, R. (2019). Conditions for the long-term preservation of a deep brine reservoir in ceres. *Geophysical Research Letters*, *46*(4), 1963–1972. https://doi.org/10.1029/2018GL081473

Castillo-Rogez & McCord, T. B. (2010). Ceres' evolution and present state constrained by shape data. *Icarus*, *205*(2), 443–459. https://doi.org/10.1016/j.icarus.2009.04.008

Christensen, N. I., & Mooney, W. D. (1995). Seismic velocity structure and composition of the continental crust: A global view [Publisher: John Wiley & Sons, Ltd]. *Journal of Geophysical Research: Solid Earth*, *100*, 9761–9788. https://doi.org/10.1029/95JB00259

De Angelis, S., Ferrari, M., De Sanctis, M., Ammannito, E., Raponi, A., & Ciarniello, M. (2021). High-temperature VIS-IR spectroscopy of NH4-phyllosilicates. *Journal of Geophysical Research: Planets*, *126*(5). https://doi.org/10.1029/2020JE006696

De Sanctis, M. C., Raponi, A., Ammannito, E., Ciarniello, M., Toplis, M. J., McSween, H. Y., Castillo-Rogez, J. C., Ehlmann, B. L., Carrozzo, F. G., Marchi, S., Tosi, F., Zambon, F., Capaccioni, F., Capria, M. T., Fonte, S., Formisano, M., Frigeri, A., Giardino, M., Longobardo, A., … Russell, C. T. (2016). Bright carbonate deposits as evidence of aqueous alteration on (1) ceres. *Nature*, *536*(7614), 54–57. https://doi.org/10.1038/nature18290

DLR. (n.d.). *Astropedia - ceres dawn FC2 HAMO global DTM 137m*. Retrieved June 5, 2024, from https://astrogeology.usgs.gov/search/map/ceres_dawn_fc2_hamo_global_dtm_137m

Ermakov, A. I., Fu, R. R., Castillo-Rogez, J. C., Raymond, C. A., Park, R. S., Preusker, F., Russell, C. T., Smith, D. E., & Zuber, M. T. (2017). Constraints on ceres' internal structure and evolution from its shape and gravity measured by the dawn spacecraft [Publisher: John Wiley & Sons, Ltd]. *Journal of Geophysical Research: Planets*, *122*(11), 2267–2293. https://doi.org/10.1002/2017JE005302

Formisano, M., Federico, C., Castillo-Rogez, J., De Sanctis, M., & Magni, G. (2020). Thermal convection in the crust of the dwarf planet - i. ceres. *Monthly Notices of the Royal Astronomical Society*, *494*(4), 5704–5712. https://doi.org/10.1093/mnras/staa1115

Fu, R. R., Ermakov, A. I., Marchi, S., Castillo-Rogez, J. C., Raymond, C. A., Hager, B. H., Zuber, M. T., King, S. D., Bland, M. T., Cristina De Sanctis, M., Preusker, F., Park, R. S., & Russell, C. T. (2017). The interior structure of ceres as revealed by surface topography. *Earth and Planetary Science Letters*, *476*, 153–164. https://doi.org/10.1016/j.epsl.2017.07.053

Goutorbe, B., Poort, J., Lucazeau, F., & Raillard, S. (2011). Global heat flow trends resolved from multiple geological and geophysical proxies. *Geophysical Journal International*, *187*(3), 1405–1419. https://doi.org/10.1111/j.1365-246X.2011.05228.x

Heiskanen, W. A., & Vening Meinesz, F. A. (1959). The earth and its gravity field. [Publisher: American Association for the Advancement of Science]. *Science*, *129*(3347), 460–460. https://doi.org/10.1126/science.129.3347.460.b

Hemingway, D. J., & Matsuyama, I. (2017). Isostatic equilibrium in spherical coordinates and implications for crustal thickness on the moon, mars, enceladus, and elsewhere [Publisher: John

Wiley & Sons, Ltd]. *Geophysical Research Letters*, *44*(15), 7695–7705. https://doi.org/10.1002/2017GL073334

Hirt, C., & Rexer, M. (2015). Earth2014: 1 arc-min shape, topography, bedrock and ice-sheet models – available as gridded data and degree-10,800 spherical harmonics. *International Journal of Applied Earth Observation and Geoinformation*, *39*, 103–112. https://doi.org/10.1016/j.jag.2015.03.001

Hollebon, J., & Fazi, F. (2020, October 27). *Efficient HRTF representation using compact mode HRTFs*.

Ice - thermal properties. (n.d.). Retrieved August 28, 2024, from https://www.engineeringtoolbox.com/ice-thermal-properties-d_576.html

King, S., Bland, M., Marchi, S., Raymond, C., Russell, C., Scully, J., & Sizemore, H. (2022). Ceres' broad-scale surface geomorphology largely due to asymmetric internal convection. *AGU Advances*, *3*(3). https://doi.org/10.1029/2021AV000571

King, S., Castillo-Rogez, J., Toplis, M., Bland, M., Raymond, C., & Russell, C. (2018). Ceres internal structure from geophysical constraints. *Meteoritics and Planetary Science*, *53*(9), 1999–2007. https://doi.org/10.1111/maps.13063

Konopliv, A., Park, R., Vaughan, A., Bills, B., Asmar, S., Ermakov, A., Rambaux, N., Raymond, C., Castillo-Rogez, J., Russell, C., Smith, D., & Zuber, M. (2018). The ceres gravity field, spin pole, rotation period and orbit from the dawn radiometric tracking and optical data. *Icarus*, *299*, 411–429. https://doi.org/10.1016/j.icarus.2017.08.005

Li, J.-Y., McFadden, L. A., Parker, J. W., Young, E. F., Stern, S. A., Thomas, P. C., Russell, C. T., & Sykes, M. V. (2006). Photometric analysis of 1 ceres and surface mapping from HST observations. *Icarus*, *182*(1), 143–160. https://doi.org/10.1016/j.icarus.2005.12.012

Lissauer, J. J., & de Pater, I. (2019). *Fundamental planetary science: Physics, chemistry and habitability*. Cambridge University Press. https://doi.org/10.1017/9781108304061

Mao, X., & McKinnon, W. B. (2018). Faster paleospin and deep-seated uncompensated mass as possible explanations for ceres' present-day shape and gravity. *Icarus*, *299*, 430–442. https://doi.org/10.1016/j.icarus.2017.08.033

Mao, Z., Fan, D., Lin, J.-F., Yang, J., Tkachev, S. N., Zhuravlev, K., & Prakapenka, V. B. (2015). Elasticity of single-crystal olivine at high pressures and temperatures. *Earth and Planetary Science Letters*, *426*, 204–215. https://doi.org/10.1016/j.epsl.2015.06.045

McCord, T. B., & Sotin, C. (2005). Ceres: Evolution and current state [Publisher: John Wiley & Sons, Ltd]. *Journal of Geophysical Research: Planets*, *110*. https://doi.org/10.1029/2004JE002244

McCord, T. B., & Zambon, F. (2019). The surface composition of ceres from the dawn mission. *The Composition of Ceres*, *318*, 2–13. https://doi.org/10.1016/j.icarus.2018.03.004

McDonough, W. F., & Yoshizaki, T. (2021). Terrestrial planet compositions controlled by accretion disk magnetic field. *Progress in Earth and Planetary Science*, *8*(1), 39. https://doi.org/10.1186/s40645-021-00429-4

Neumann, W., Jaumann, R., Castillo-Rogez, J., Raymond, C., & Russell, C. (2020). Ceres' partial differentiation: Undifferentiated crust mixing with a water-rich mantle. *Astronomy and Astrophysics*, *633*. https://doi.org/10.1051/0004-6361/201936607

Neumann, W., Breuer, D., & Spohn, T. (2015). Modelling the internal structure of ceres: Coupling of accretion with compaction by creep and implications for the water-rock differentiation [ISBN: 0004-6361 Publisher: EDP Sciences]. *Astronomy & Astrophysics*, *584*, A117.

Neumeier, J. J. (2018). Elastic constants, bulk modulus, and compressibility of h2o ice ih for the temperature range 50 k–273 k. *Journal of Physical and Chemical Reference Data*, *47*(3), 033101. https://doi.org/10.1063/1.5030640

Neveu, M., & Desch, S. J. (2015). Geochemistry, thermal evolution, and cryovolcanism on ceres with a muddy ice mantle [Publisher: John Wiley & Sons, Ltd]. *Geophysical Research Letters*, *42*(23), 10, 197–10, 206. https://doi.org/10.1002/2015GL066375

Olivine mineral data. (n.d.). Retrieved June 5, 2024, from https://webmineral.com/data/Olivine.shtml

Osako, M., Yoneda, A., & Ito, E. (2010). Thermal diffusivity, thermal conductivity and heat capacity of serpentine (antigorite) under high pressure. *Special Issue on Deep Slab and Mantle Dynamics*, *183*(1), 229–233. https://doi.org/10.1016/j.pepi.2010.07.005

Park, R. S., Konopliv, A. S., Bills, B. G., Rambaux, N., Castillo-Rogez, J. C., Raymond, C. A., Vaughan, A. T., Ermakov, A. I., Zuber, M. T., Fu, R. R., Toplis, M. J., Russell, C. T., Nathues, A., & Preusker,

F. (2016). A partially differentiated interior for (1) ceres deduced from its gravity field and shape. *Nature*, *537*(7621), 515–517. https://doi.org/10.1038/nature18955

Quick, L. C., Buczkowski, D. L., Ruesch, O., Scully, J. E., Castillo-Rogez, J., Raymond, C. A., Schenk, P. M., Sizemore, H. G., & Sykes, M. V. (2019). A possible brine reservoir beneath occator crater: Thermal and compositional evolution and formation of the cerealia dome and vinalia faculae. *Occator Crater on Ceres*, *320*, 119–135. https://doi.org/10.1016/j.icarus.2018.07.016

Ruesch, O., Genova, A., Neumann, W., Quick, L., Castillo-Rogez, J., Raymond, C., Russell, C., & Zuber, M. (2019). Slurry extrusion on ceres from a convective mud-bearing mantle. *Nature Geoscience*, *12*(7), 505–509. https://doi.org/10.1038/s41561-019-0378-7

Ruesch, O., Platz, T., Schenk, P., McFadden, L. A., Castillo-Rogez, J. C., Quick, L. C., Byrne, S., Preusker, F., O'Brien, D. P., & Schmedemann, N. (2016). Cryovolcanism on ceres [ISBN: 0036-8075 Publisher: American Association for the Advancement of Science]. *Science*, *353*(6303), aaf4286.

Sori, M. M., Byrne, S., Bland, M. T., Bramson, A. M., Ermakov, A. I., Hamilton, C. W., Otto, K. A., Ruesch, O., & Russell, C. T. (2017). The vanishing cryovolcanoes of ceres [ISBN: 0094-8276 Publisher: Wiley Online Library]. *Geophysical Research Letters*, *44*(3), 1243–1250.

Stein, N., Ehlmann, B., Palomba, E., De Sanctis, M., Nathues, A., Hiesinger, H., Ammannito, E., Raymond, C., Jaumann, R., Longobardo, A., & Russell, C. (2019). The formation and evolution of bright spots on ceres. *Occator Crater on Ceres*, *320*, 188–201. https://doi.org/10.1016/j.icarus.2017.10.014

Szwillus, W., Afonso, J. C., Ebbing, J., & Mooney, W. D. (2019). Global crustal thickness and velocity structure from geostatistical analysis of seismic data [Publisher: John Wiley & Sons, Ltd]. *Journal of Geophysical Research: Solid Earth*, *124*(2), 1626–1652. https://doi.org/10.1029/2018JB016593

Thomas, P. C., Parker, J. W., McFadden, L. A., Russell, C. T., Stern, S. A., Sykes, M. V., & Young, E. F. (2005). Differentiation of the asteroid ceres as revealed by its shape. *Nature*, *437*(7056), 224–226. https://doi.org/10.1038/nature03938

Tricarico, P. (2014). MULTI-LAYER HYDROSTATIC EQUILIBRIUM OF PLANETS AND SYNCHRONOUS MOONS: THEORY AND APPLICATION TO CERES AND TO SOLAR SYSTEM MOONS [Publisher: The American Astronomical Society]. *The Astrophysical Journal*, *782*(2), 99. https://doi.org/10.1088/0004-637X/782/2/99

Vu, T. H., Hodyss, R., Johnson, P. V., & Choukroun, M. (2017). Preferential formation of sodium salts from frozen sodium-ammonium-chloride-carbonate brines – implications for ceres' bright spots. *Planetary and Space Science*, *141*, 73–77. https://doi.org/10.1016/j.pss.2017.04.014

Watts, A. B., & Moore, J. D. P. (2017). Flexural isostasy: Constraints from gravity and topography power spectra [Publisher: John Wiley & Sons, Ltd]. *Journal of Geophysical Research: Solid Earth*, *122*(10), 8417–8430. https://doi.org/10.1002/2017JB014571

Zolotov, M. Y. (2009). On the composition and differentiation of ceres. *Icarus*, *204*(1), 183–193. https://doi.org/10.1016/j.icarus.2009.06.011